

1 **Rapid recycling of glutamate transporters on the astroglial surface**

2

3 Piotr Michaluk<sup>\*1,2</sup>, Janosch P. Heller<sup>1,3</sup>, Dmitri A. Rusakov<sup>1\*</sup>

4

5 <sup>1</sup> Queen Square UCL Institute of Neurology, University College London, Queen  
6 Square, London WC1N 3BG, U.K.

7 <sup>2</sup> BRAINCITY, Nencki Institute of Experimental Biology PAS, 3 Pasteur Street, 02-093  
8 Warszawa, Poland

9 <sup>3</sup> School of Biotechnology and National Institute for Cellular Biotechnology (NICB),  
10 Dublin City University, Glasnevin, Dublin 9, Ireland

11

12

13

14

15

16

17 Correspondence: Dmitri A. Rusakov ([d.rusakov@ucl.ac.uk](mailto:d.rusakov@ucl.ac.uk)) or Piotr Michaluk  
18 ([p.michaluk@nencki.edu.pl](mailto:p.michaluk@nencki.edu.pl))

19 **ABSTRACT**

20 Glutamate uptake by astroglial transporters confines excitatory transmission to the  
21 synaptic cleft. The efficiency of this mechanism depends on the transporter dynamics  
22 in the astrocyte membrane, which remains poorly understood. Here, we visualise the  
23 main glial glutamate transporter GLT1 by generating its pH-sensitive fluorescent  
24 analogue, GLT1-SEP. FRAP-based imaging shows that 70-75% of GLT1-SEP dwell  
25 on the surface of rat brain astroglia, recycling with a lifetime of ~22 s. Genetic deletion  
26 of the C-terminus accelerates GLT1-SEP membrane turnover while disrupting its  
27 surface pattern, as revealed by single-molecule localisation microscopy. Excitatory  
28 activity boosts surface mobility of GLT1-SEP, involving its C-terminus, metabotropic  
29 glutamate receptors, intracellular  $\text{Ca}^{2+}$  and calcineurin-phosphatase activity, but not  
30 the broad-range kinase activity. The results suggest that membrane turnover, rather  
31 than lateral diffusion, is the main 'redeployment' route for the immobile fraction (20-  
32 30%) of surface-expressed GLT1. This finding reveals an important mechanism  
33 helping to control extrasynaptic escape of glutamate.

34

## 35 INTRODUCTION

36 Excitatory transmission in the brain occurs mainly through the release of glutamate at  
37 chemical synapses. Once released, glutamate is taken up by high-affinity transporters  
38 that densely populate the plasma membrane of brain astrocytes (Wadiche et al.,  
39 1995a; Danbolt, 2001). The main glial glutamate transporter GLT1 (EAAT2) maintains  
40 extracellular glutamate at nanomolar levels, thus constraining its excitatory action  
41 mainly to the synaptic cleft (Moussawi et al., 2011; Zheng and Rusakov, 2015).  
42 Because synaptic vesicles release ~3000 glutamate molecules (Savtchenko et al.,  
43 2013) and because glutamate uptake cycle can take tens of milliseconds (Wadiche et  
44 al., 1995b), large numbers of transporter molecules have to be available near  
45 synapses to buffer the escaping glutamate (Lehre and Danbolt, 1998; Bergles et al.,  
46 2002). Indeed, the high occurrence of GLT1 in astroglial plasma membranes (Danbolt,  
47 2001) ensures that regular network activity does not overwhelm glutamate transport  
48 (Bergles and Jahr, 1998; Diamond and Jahr, 2000). However, intense excitation can  
49 prompt glutamate escape from the immediate synapse, leading to activation of  
50 extrasynaptic receptors or even neighbouring synapses (Lozovaya et al., 1999; Arnth-  
51 Jensen et al., 2002; Scimemi et al., 2004; Henneberger et al., 2020; Kopach et al.,  
52 2020). Ultimately, the reduced availability of GLT1 in the synaptic environment has  
53 long been associated with pathologic conditions such as neurodegenerative diseases,  
54 stroke, or addiction (Maragakis and Rothstein, 2004; Fontana, 2015; Kruyer et al.,  
55 2019).

56 These considerations prompted intense interest in the cellular mechanisms underlying  
57 cellular trafficking and turnover of astroglial and neuronal glutamate transporters. A  
58 growing body of evidence has suggested the involvement of its carboxyl-terminal  
59 domain and protein kinase C (Kalandadze et al., 2002; Gonzalez et al., 2007) and  
60 calmodulin-dependent protein kinase (Underhill et al., 2015), also engaging ubiquitin-  
61 dependent processes (Gonzalez et al., 2007; Gonzalez-Gonzalez et al., 2008;  
62 Martinez-Villarreal et al., 2012) and constitutive protein sumoylation (Garcia-Tardon et  
63 al., 2012; Foran et al., 2014; Piniella et al., 2018). Ultimately, these findings unveil the  
64 potential to regulate long-term, systemic changes in the GLT1 expression in a  
65 therapeutic context (reviewed in (Fontana, 2015; Peterson and Binder, 2019)).  
66 However, what happens to GLT1 trafficking on the time scale of the ongoing brain  
67 activity remains poorly understood. In recent elegant studies, single-particle tracking

68 with quantum dots (QDs) has detected high surface mobility of GLUT1 in astroglia  
69 (Murphy-Royal et al., 2015; Al Awabdh et al., 2016). Lateral diffusivity of transporters  
70 was boosted by local glutamatergic activity, thus suggesting the use-dependent  
71 surface supply of GLUT1 towards active synapses (Murphy-Royal et al., 2015; Al  
72 Awabdh et al., 2016). However, synthetic QDs almost certainly prevent their link-  
73 labelled molecules from the membrane-intracellular compartment turnover and, at the  
74 same time, do not label any newly appearing molecules on the cell surface. Thus, the  
75 molecule-tracking observations relying solely on QDs could miss important changes in  
76 the composition and/or mobility of the studied molecular species due to their  
77 continuous recycling in the membrane.

78 We therefore set out to develop an approach enabling us to document, in real time,  
79 the exchange between membrane and intracellular fractions of GLUT1, in addition to  
80 monitoring its lateral diffusion on the cell surface. To achieve this, we generated a fully  
81 functional variant of GLUT1, termed GLUT1-SEP, by adding an extracellular fragment  
82 with the pH-sensitive, Super-Ecliptic pHluorin (SEP); GLUT1-SEP fluoresces when  
83 exposed to the extracellular but not in low pH of intracellular compartments.  
84 Expressing GLUT1-SEP in astroglia in cell cultures and brain slices allowed us to  
85 combine the optical protocols of fluorescence recovery after photobleaching (FRAP)  
86 with molecular and pharmacological dissection, to monitor membrane turnover and  
87 lateral diffusion of the transporter proteins.

88

## 89 **RESULTS**

### 90 **Developing and probing GLUT1-SEP**

91 First, we designed the GLUT1-SEP probe for FRAP measurements by introducing SEP  
92 into the second intracellular loop of GLUT1a, between two proline residues (P199 and  
93 P200). GLUT1a was selected because it accounts for 90% of total GLUT1 expression in  
94 astrocytes in the rat brain, with GLUT1b and GLUT1c accounting for ~6% and ~1%,  
95 respectively (Holmseth et al., 2009). Next, aiming at astrocyte-specific expression we  
96 cloned the construct under the gfaABC<sub>1</sub>D promoter (Lee et al., 2008) (Figure 1A;  
97 Materials and Methods).

98 To test if this new construct (termed GLT1-SEP thereafter) is a functional glutamate  
99 transporter we transfected with it HEK 293T cells, which do not normally express  
100 GLT1. The control group of cells was transfected with the plasmid coding wild-type  
101 GLT1. For identification purposes, and to keep the same plasmid concentrations, cells  
102 were co-transfected with GLT1 constructs and mRFP1 under  $\beta$ -actin promoter, at a  
103 2:1 ratio. Next, in whole-cell mode we recorded uptake currents in transfected cells  
104 induced by a 1 s application of 1 mM glutamate through a theta-glass solution-  
105 exchange system (Figure 1B), the method that avoids any mechanical concomitants of  
106 the application protocol (Sylantsev and Rusakov, 2013). Systematic recording across  
107 holding voltages produced normalized I-V curves that showed an excellent match  
108 between the wild-type native transporter and the mutant (Figure 1 C). However, the  
109 absolute current in GLT1-SEP expressing cells was on average ~50% lower (Figure 1  
110 - figure supplement 1A), possibly because of the lower expression compared to native  
111 GLT1.

112 To understand further the relationship between the expression levels of native GLT1  
113 and GLT1-SEP in HEK cells, we firstly compared immuno-staining in cells expressing  
114 GLT1 or GLT1-SEP, and found that GLT1-SEP staining was indeed significantly lower  
115 (Figure 1 - figure supplement 2A-B). Secondly, we compared expression of GLT1  
116 variants in HEK cells using quantitative western blot (normalised against  $\alpha$ -tubulin; n =  
117 6 samples per condition). In these samples, GLT1 expression was twice as high as  
118 that of GLT1-SEP, and genetic deletion of the intracellular C-terminus (GLT1 $\Delta$ C-SEP  
119 variant) did not change this difference significantly (Figure 1 - figure supplement 2C-  
120 D). Thus, the decrease in the surface expression of GLT1-SEP and in its transporter  
121 current in HEK cells (compared with the case of wild-type GLT1) were matched,  
122 suggesting that adding the extracellular SEP tag had no detectable effect on  
123 glutamate uptake properties of GLT1.

124

### 125 **Intracellular versus membrane fractions of GLT1-SEP in astroglia**

126 We next expressed GLT1-SEP in mixed cultures of neurons and glial cells. Thanks to  
127 the *gfaABC1D* promoter, the probe was almost exclusively expressed in astrocytes.  
128 The living GLT1-SEP expressing cells were readily visualised, featuring a dense and  
129 homogenous expression pattern that reveals fine detail of cell morphology (Figure 1D,

130 upper left). Because the pH-sensitive GLT1-SEP fluoresces at higher extracellular pH  
 131 but not at lower pH in intracellular compartments, we were able to estimate directly its  
 132 membrane and intracellular fractions. Firstly, we confirmed that the observed  
 133 fluorescence comes mainly from the membrane fraction of GLT-SEP. Indeed, brief  
 134 acidification of the extracellular medium to pH 5.5 (10 second pipette puff with pH-  
 135 adjusted bath medium) reversibly suppressed GLT1-SEP fluorescence (Figure 1D,  
 136 upper row). Conversely, proton permeation of the cell membrane (10 second puff with  
 137 NH<sub>4</sub>Cl) could reveal both intra- and extracellular GLT1-SEP fractions, in a reversible  
 138 fashion (Figure 1D, lower row). Systematic quantification of these experiments (Figure  
 139 1E) provided an estimate of the average GLT1-SEP surface fraction in astroglial  
 140 processes,  $R = 0.72 \pm 0.18$  ( $n = 8$  cells, Figure 1F). In other words, between 2/3 and  
 141 3/4 of all cellular GLT1-SEP were exposed to the extracellular space. The  $R$  estimate  
 142 for the cell soma was somewhat lower (Figure 1F), but because exact identification of  
 143 the somatic boundaries was ambiguous, we did not use somatic data in further  
 144 analyses.

145 These data provided an important constraint for a (steady-state) quantitative  
 146 assessment of the GLT1-SEP turnover kinetics. Introducing the membrane-

147 intracellular exchange reaction (Figure 1 -figure supplement 1B) as  $C_{in} \xrightleftharpoons[k_{-1}]{k_1} C_{mem}$

148 ( $C_m$  and  $C_{in}$  are membrane and intracellular concentration of GLT1-SEP, respectively)

149 leads to a direct relationship between the corresponding kinetic constants  $k_1$  and  $k_{-1}$

150 (Figure 1 -figure supplement 1C):  $k_{-1} = \left(\frac{1}{R} - 1\right)k_1 = 0.389k_1$ .

151 Again, to understand better how transfected and non-transfected astroglia express  
 152 GLT1 variants, we stained transfected astrocytes with GFP in the green channel while  
 153 using an antibody against GLT1 C-terminus in the red channel. We were thus able to  
 154 compare all-variant GLT1 expression in the astrocytes transfected with GLT1-SEP ( $n$   
 155 = 29) with GLT1 expression in the neighbouring, non-transfected cells Figure 1 - figure  
 156 supplement 3A). In the transfected astrocytes, the all-variant GLT1 level was higher  
 157 than in non-transfected cells (Figure 1 - figure supplement 3B). In the astrocytes  
 158 transfected with GLT1 $\Delta$ C-SEP ( $n = 27$ ) we were able to detect only endogenous GLT1  
 159 levels as the antibody does not recognize GLT1 $\Delta$ C-SEP. In the transfected astrocytes,  
 160 GLT1 level was 25-50% higher than that for GLT1 in non-transfected cells (Figure 1 -

161 figure supplement 3B). We also confirmed that the endogenous GLT1 expression was  
162 perfectly stable in non-transfected cells that are present in transfected culture samples  
163 (Figure 1 - figure supplement 3C). These immunostaining data have simply confirmed  
164 that the membranes of both transfected and non-transfected cells are densely and  
165 relatively uniformly packed with the respective GLT1 variants.

166 Although the steady-state data obtained here are key for understanding the  
167 relationship between intracellular and membrane fractions of GLT1, they could not on  
168 their own reveal the actual rate of GLT1-SEP turnover in the cell membrane. To  
169 address this, we implemented a different approach, as described below.

170

### 171 **GLT1-SEP recycling in the plasma membrane**

172 Because photobleaching quenches irreversibly only the fluorophores that are in the  
173 excited (fluorescent) state, it could be used to separate the fluorescent from the non-  
174 fluorescent GLT1-SEP fraction. We therefore implemented a two-photon excitation  
175 FRAP protocol in which photobleaching applies virtually to the entire astrocyte  
176 expressing GLT1-SEP (Figure 2A). This was feasible mainly because the morphology  
177 of cultured astroglia was essentially two-dimensional, thus permitting comprehensive  
178 photobleaching in close proximity of the focal plane. Thus, we used a 'Tornado' laser  
179 scan mode, a spiral line-scan that could effectively cover a circular region over just 1-2  
180 ms (Jensen et al., 2019), to almost entirely suppress GLT1-SEP fluorescence within  
181 the target area (Figure 2A, dashed green spiral; area also shown by dashed red  
182 circles). This approach enabled us to document partial fluorescence recovery within  
183 smaller ROIs inside the bleached area: sampling normally included three ~10  $\mu\text{m}$  wide  
184 circular ROIs over cell processes (and additionally one ~20  $\mu\text{m}$  ROI over the soma) in  
185 each cell (Figure 2A, dotted orange circles). The ROI selection was restricted to  
186 morphologically homogenous cell areas inside the fully bleached territory, but  
187 otherwise was quasi-random (three ROIs picked randomly out of 10-20 available per  
188 cell). These experiments produced the average FRAP time course, with relatively low  
189 noise (Figure 2B). The cellular biophysical mechanisms underpinning this time course  
190 combine membrane insertion of non-bleached GLT1-SEP and, if any, residual  
191 photobleaching of surface-bound GLT1-SEP. Solving the corresponding kinetic  
192 equations (Figure 2 -figure supplement 1) provide the resulting fluorescence time

193 course as  $C_{mem}^f = RC_{in} (e^{-k_b t} - e^{-k_1 t})$  where  $t$  is time and  $k_b$  is the residual  
194 photobleaching constant (other notations as above). This equation has two orthogonal  
195 (independent) free parameters,  $C_{in}$  and  $k_1$ , whereas the residual photobleaching rate  
196  $k_b$  turned out to be negligible throughout the sample. The best-fit estimate gave  
197 (Figure 2B):  $k_1 = 0.045 \pm 0.003 \text{ s}^{-1}$ ,  $k_{-1} = 0.020 \pm 0.001 \text{ s}^{-1}$ , and  $C_{in} = 0.30 \pm 0.01$ .  
198 Reassuringly, the value of  $C_{in}$  (intracellular fraction of GLT1-SEP) obtained in these  
199 experiments was indistinguishable from the value of  $1 - R = 0.28$  obtained using a fully  
200 independent proton permeation method (Figure 1F).

201 These estimates suggest that the characteristic lifetime of the membrane GLT1-SEP  
202 fraction, as given by  $k_1^{-1}$ , is  $\sim 22$  seconds. Because the cytosolic carboxy-terminal  
203 domain of GLT1 has earlier been implicated in the GLT1 expression mechanism (Gibb  
204 et al., 2007; Foran et al., 2014), we asked whether it interferes with the membrane  
205 kinetics of the transporter. We therefore expressed GLT1 $\Delta$ C-SEP in astroglia. FRAP  
206 experiments in the GLT1 $\Delta$ C-SEP expressing cells (Figure 2C) showed that deleting  
207 the C-terminus had only a moderate effect on the intracellular fraction of transporters  
208 ( $C_{in} = 0.35 \pm 0.01$ ) but reduced the GLT1 membrane lifetime by nearly a half (to  $\sim 14$   
209 s). This finding suggests that the C-terminus could play an important role in retaining  
210 GLT1 in the plasma membrane, even though a steady-state membrane-intracellular  
211 compartment ratio remains almost unaffected.

212 Do the cell-average values of the GLT1-SEP membrane fraction (and hence turnover  
213 rate) occur homogeneously throughout the cell morphology? To understand this, we  
214 directly compared distributions of the membrane and the intracellular populations of  
215 GLT1-SEP: the latter was obtained by subtracting the surface GLT1-SEP image from  
216 the total GLT1-SEP image (under  $\text{NH}_4\text{Cl}$ , as in Figure 1D). Intriguingly, this  
217 comparison revealed that the membrane GLT1-SEP does not necessarily predict the  
218 intracellular GLT1-SEP pattern which could display prominent clustering features  
219 (Figure 2D). Thus, at least in some cases the membrane dynamics of GLT1 could be  
220 specific to microscopic regions of the cell.

221

222 **Nanoscale distribution of GLT1 species with respect to synapses**



223 While FRAP measures live GLUT1 turnover in the astrocyte membrane, it does not  
224 reveal surface distribution of these molecules, in particular that with respect to  
225 synaptic connections. We therefore turned to super-resolution single-molecule  
226 localisation microscopy (SMLM) that involves stochastic localisation of individual  
227 molecules (van de Linde et al., 2011) using multi-colour 3D SMLM experimental  
228 protocols that we have established previously (Heller et al., 2017; Heller and Rusakov,  
229 2019; Heller et al., 2020) (Materials and Methods). We thus used chromatically  
230 separable photoswitchable dyes to visualise distributions of the native GLUT1, mutant  
231 GLUT1-SEP, or GLUT1 $\Delta$ C-SEP species and their relationship to the synaptic clusters of  
232 the ubiquitous postsynaptic density protein PSD95 in mixed cultures (Figure 3A,  
233 Figure 3 -figure supplement 1A; as this method used permeabilization, 25-30% of the  
234 label reflected the intracellular fraction of GLUT1).

235 Visualisation with SMLM revealed that the scatter of wild-type GLUT1 tends towards  
236 forming clusters, both among GLUT1 molecules and also between GLUT1 and PSD95,  
237 and that GLUT1-SEP-expressing cells display similar features (Figure 3B). Indeed, the  
238 classical nearest-neighbour analysis indicated that the pattern of wild-type GLUT1 and  
239 GLUT1-SEP with respect to PSD95 clusters deviates from the evenly random  
240 distribution towards closer spatial association (Figure 3C), and that these transporter  
241 molecules also tend to form short-distance (up to 50 nm) clusters among themselves  
242 (Figure 3 -figure supplement 1B). In contrast, the species with deleted C-terminus,  
243 GLUT1 $\Delta$ C-SEP, showed spatial dissociation (distancing) with PSD95 clusters (Figure  
244 3B-C) while displaying dense molecular clustering among themselves, to the extent  
245 that the latter is not distinguishable from uniform packing at a high local density  
246 (Figure 3 -figure supplement 1B; this analysis does not cover higher-order, longer-  
247 distance GLUT1 $\Delta$ C-SEP clustering, which is evident in Figure 3B). These observations  
248 indicate that the C-terminus of GLUT1 plays a critical role not only in its cellular  
249 membrane turnover but also in the surface (and submembrane) expression pattern of  
250 the protein.

251

## 252 **Lateral mobility of GLUT1-SEP in astroglia**

253 We next set out to assess lateral surface mobility of GLUT1-SEP using a classical  
254 FRAP protocol, in which the fluorescence kinetics is monitored within a small ROI

255 (Figure 4A). Because running a FRAP protocol bleaches immobile molecules that  
256 remain within the ROI, repeating this protocol within the same ROI may produce a  
257 different FRAP time course. To account for this and any other use-dependent trends in  
258 the imaging conditions, we routinely recorded pairs of FRAP trials separated by 1 min  
259 (Figure 4B, Figure 4 -figure supplement 1), unless indicated otherwise. This time  
260 interval was also longer than the GLT1 membrane turnover period (~22 s, see above),  
261 which should help minimise the number of bleached immobile molecules remaining  
262 within the ROI, as they are replaced by new arrivals from the intracellular  
263 compartment. This approach enabled us to compare FRAP kinetics between control  
264 conditions and during ligand application, in the manner that provides correction for any  
265 consistent difference within paired FRAP trials (Figure 4C, Figure 4 -figure supplement  
266 1).

267 In the first experiment, we therefore documented FRAP kinetics within a small (~1.6  
268  $\mu\text{m}$  diameter) circular membrane area of a visualised astrocyte, in baseline conditions  
269 and during a brief (250 ms, 1 mM) application of glutamate 200 ms prior to bleaching  
270 onset, to mimic a transient rise in local excitatory activity.

271 The data (corrected for paired-trial trends) showed a clear difference in the FRAP  
272 kinetics between the two conditions (Figure 4D, left). This could reflect a difference in  
273 lateral diffusivity of mobile transporters, but also in the immobile versus mobile  
274 fractions of GLT1-SEP. To evaluate both variables from the FRAP kinetics, we used  
275 the well-established Soumpasis approach for circular ROIs (Soumpasis, 1983; Kang et  
276 al., 2009) (Materials and Methods). This fitting method operates with only two mutually  
277 independent (orthogonal) free parameters, mobile fraction  $C_{mob}$  and diffusion  
278 coefficient  $D$ , and its estimates should not depend on residual changes in  
279 fluorescence, such as photobleaching (Soumpasis, 1983; Kang et al., 2009).

280 In baseline conditions, the best-fit values were  $C_{mob} = 0.76 \pm 0.01$  and mobile-fraction  
281 diffusivity  $D = 0.152 \mu\text{m}^2/\text{s}$  (diffusion time  $\tau_D = 1.75 \pm 0.03$ , Materials and Methods),  
282 thus giving the average diffusivity (accounting for mobile and immobile molecules)  $D^*$   
283  $= C_{mob} \cdot D = 0.114 \mu\text{m}^2/\text{s}$  (Figure 4D, right). This value appears in correspondence with  
284 the average lateral diffusivity of GLT1 measured earlier with QDs (Murphy-Royal et al.,  
285 2015), although it is higher than the values reported using a different QD approach (Al  
286 Awabdh et al., 2016). When glutamate was briefly applied immediately before and  
287 after the photobleaching pulse, diffusivity of the mobile-fraction only did not appear to

288 be affected ( $\tau_D = 1.73 \pm 0.03$ ) whereas its size increased significantly ( $C_{mob} = 0.88 \pm$   
289  $0.003$ ), giving average  $D^* = 0.135 \mu\text{m}^2/\text{s}$ , an increase of  $\sim 18\%$  compared to control  
290 (Figure 4D, right). This result suggested that glutamatergic activity could boost overall  
291 membrane mobility of GLT1 transporters, a conclusion similar to that drawn earlier  
292 using QDs (Murphy-Royal et al., 2015; Al Awabdh et al., 2016).

293

## 294 **Molecular regulators of activity-dependent membrane mobility of GLT1**

295 We next found that deleting the C-terminus of GLT1-SEP does not alter its mobility in  
296 basal conditions ( $C_{mob} = 0.815 \pm 0.003$ ;  $D^* = 0.117 \mu\text{m}^2/\text{s}$ ) but appears to block the  
297 mobility-boosting effect of glutamate application (Figure 4E). A similar result was  
298 obtained when metabotropic glutamate receptors were blocked by a pharmacological  
299 cocktail: no detectable effect on GLT1-SEP mobility in baseline conditions ( $C_{mob} =$   
300  $0.795 \pm 0.003$ ;  $D^* = 0.121 \mu\text{m}^2/\text{s}$ ) but suppression of the glutamate-induced mobility  
301 increase (Figure 4F). Because purinergic receptors mediate a major signalling  
302 cascade in brain astroglia (Verkhratsky and Nedergaard, 2018), we asked whether  
303 ATP application alters mobility of GLT1-SEP, and detected no effect (Figure 4G).

304 Finally, to assess sensitivity and the dynamic range of our FRAP protocol we cross-  
305 linked surface GLT-SEP, by incubating cultures briefly (10 min in humidified incubator)  
306 with either IgY antibody (100  $\mu\text{g}/\text{ml}$ , chicken polyclonal, Merck AC146) or with the anti-  
307 GFP antibody (100  $\mu\text{g}/\text{ml}$ , chicken polyclonal, Abcam ab13970). The cross-linkage  
308 reduced the FRAP-measured transporter mobility five-fold (Figure 4H), confirming high  
309 sensitivity and general suitability of the present FRAP method.

310

## 311 **Cellular mechanisms affecting GLT1 mobility in hippocampal slices**

312 Whilst cultured astroglia are thought to retain key molecular mechanisms acting in situ,  
313 astrocytes in organised brain tissue have distinct morphology and engage in network  
314 signalling exchange that may be different from cultures. We therefore set out to  
315 validate our key observations focusing on area CA1 astroglia in organotypic  
316 hippocampal slices: these cells closely resemble their counterparts in vivo (Figure 5A),  
317 and are embedded in a well-defined synaptic circuitry. To induce a rapid rise in the  
318 spontaneous excitatory activity of the native network, we blocked GABA<sub>A</sub> receptors

319 and potassium channels with bicuculline and 4-AP (rather than applying glutamate,  
320 Figure 5B).

321 Because the morphology of astroglia in brain tissue is essentially three-dimensional,  
322 the whole-cell FRAP protocols (as in Figure 2A) were not technically feasible.

323 However, the small-ROI FRAP experiments (as in Figure 4A) in slices showed that  
324 diffusivity of GLT1-SEP in the plasma membrane was similar, if somewhat slower,  
325 than that in cultures (Figure 5C). Elevated excitatory activity increased GLT1-SEP  
326 mobility, which could be reversed by blocking spiking activity with TTX (Figure 5C).

327 We confirmed that this effect was not due to some unknown concomitants of  
328 increased network activity that might affect astrocyte membrane properties per se: a  
329 truncated sham-protein probe carrying an extracellular SEP domain showed no  
330 changes in lateral diffusion under this protocol (Figure 5-figure supplement 1A).

331 Conversely, application of the vehicle DMSO on its own had no effect on the activity-  
332 dependent increase in GLT1-SEP diffusion (Figure 5-figure supplement 1B).

333 Again, deletion of the C-terminus or the pharmacological blockade of metabotropic  
334 glutamate receptors suppressed the activity-dependent mobility increase (Figure 5D-  
335 E). Because metabotropic glutamate receptors engage a major  $Ca^{2+}$  signalling  
336 cascade in astroglia (Porter and McCarthy, 1997), we asked if buffering intracellular  
337  $Ca^{2+}$  with BAPTA-AM is involved, and found this to be the case (Figure 5F).

338 Investigating this further, we blocked the calcium and calmodulin-dependent  
339 phosphatase calcineurin, which produced similar suppression (Figure 5G). However,  
340 non-selective protein kinase inhibition with the antibiotic staurosporine left the  
341 excitation-induced rise of GLT1-SEP mobility intact (Figure 5H), thus narrowing the  
342 range of the candidate molecular mechanisms involved.

343 Throughout these experiments, we compared GLT-1 mobility before and after LP-4  
344 application, under exactly the same pharmacological challenge. At the same time, the  
345 pharmacological manipulations per se had no detectable influence on the prominent  
346 boosting effect of 4-AP on network activity (as in Fig. 5B). We therefore considered  
347 that, in the present experimental design, any concomitant effects of drug application  
348 on neurons were largely cancelled out, for comparison purposes.

349

350 **DISCUSSION**

351 Here, we developed a functional fluorescent analogue of the main glial glutamate  
352 transporter GLT1, termed GLT1-SEP, and used it to evaluate its membrane dynamics,  
353 incorporating both surface mobility and membrane-intracellular compartment turnover  
354 in astrocytes. We used patch-clamp electrophysiology, immunostaining assays, and  
355 super-resolution SMLM imaging to confirm that glutamate transport properties of  
356 GLT1-SEP and its cell expression are generally compatible with its wild-type  
357 counterpart. Clearly, virtually any direct experimental intervention, such as patch-  
358 clamp, genetically encoded sensors, opsins, or fluorescent tags, by definition  
359 introduce some perturbation to the system, which is difficult to control entirely.  
360 However, FRAP applied to fluorophore-fused proteins has for decades proved a key  
361 method to grasp accurately their membrane kinetics, and fluorescent tagging has been  
362 successfully implemented in recent protein turnover studies (Rudolph et al., 2019).  
363 Our live-imaging and immunostaining data also indicate that the expression of GLT1-  
364 SEP was consistently dense and relatively even across the astrocyte surface, similar  
365 to that of native GLT1, which argues for physiological relevance of our approach.

366 Taking advantage of the pH-sensitive fluorescence and photobleaching properties of  
367 GLT1-SEP, we established that the 70-75% fraction of its cellular content reside on  
368 the astrocyte surface, with a characteristic turnover rate of 0.04-0.05 s<sup>-1</sup>, which  
369 corresponds to a 20-25 s cycle. That the population of functional astroglial glutamate  
370 transporters is effectively replaced several times per minute must be an intriguing  
371 discovery. Interestingly, a recent study used fixed-tissue immunocytochemistry in pure  
372 astroglial cultures to find only ~25% of all GLT1 expressed in the cell membrane  
373 (Underhill et al., 2015), thus relating a boost in transporter numbers to the presence of  
374 neuronal connections (in the mixed cultures slices employed here).

375 Removing the C-terminus of GLT1-SEP only moderately increased its intracellular  
376 fraction while substantially reducing its plasma membrane lifetime. These observations  
377 suggest an important contribution of the C-terminus to the retaining of GLT1 molecules  
378 on the astrocyte surface. Intriguingly, SMLM imaging revealed that deletion of the C-  
379 terminus severely disrupts the cell surface pattern of GLT1 and its spatial relationship  
380 with neighbouring synaptic connections (represented by clusters of PSD95).

381 It has previously been shown that GLT1 is endocytosed constitutively, in a clathrin-  
382 dependent manner, taking the transporter into rapidly-recycling endosomes containing  
383 EEA1 and Rab4 (Martinez-Villarreal et al., 2012). Earlier studies have also indicated

384 that the common neuronal glutamate transporter GLAST also undergoes clathrin-  
385 dependent endocytosis (Gonzalez et al., 2007). Using reversible biotinylation followed  
386 by immunocytochemistry, Robinson's group obtained estimates of the membrane  
387 residence time of EEAT1 (Fournier et al., 2004), and subsequent studies identified  
388 several molecular cascades that control cell surface expression of GLAST and GLT1  
389 including ubiquitination and sumoylation (Gonzalez et al., 2007; Garcia-Tardon et al.,  
390 2012; Martinez-Villarreal et al., 2012; Piniella et al., 2018). While the biochemical  
391 machinery of GLT1 turnover is outside the scope of the present study, its investigation  
392 should provide further insights into the adaptive features of glutamate transport in the  
393 brain.

394 We next employed GLT1-SEP to investigate its lateral mobility in the plasma  
395 membrane, and the regulatory mechanisms involved. A similar question has been  
396 elegantly explored in two studies using single-particle tracking with QDs (Murphy-  
397 Royal et al., 2015; Al Awabdh et al., 2016). However, the key advantage of the  
398 present approach is that it accounts for membrane-intracellular compartment  
399 exchange, in addition to lateral mobility per se: tracking QD-labelled GLT1 must ignore  
400 the non-labelled GLT1 fraction that is being constantly delivered to the cell surface.  
401 We found relatively high average lateral diffusivity ( $0.10\text{-}0.15\ \mu\text{m}^2/\text{s}$ ), but also a  
402 significant fraction of immobile transporters (25-30%). Importantly, the characteristic  
403 lateral diffusion time of the GLT1-SEP mobile fraction ( $\sim 1.75\ \text{s}$ ) was much shorter than  
404 its membrane lifetime of ( $\sim 22\ \text{s}$ ). This implies that the assessment of mobile  
405 transporter diffusivity, obtained here with GLT1-SEP or earlier with QDs, should not be  
406 noticeably influenced by its membrane turnover. Nonetheless, the latter could have a  
407 critical effect on the dynamics of the immobile (slowly moving) fraction of GLT1. For  
408 instance, the earlier studies found that GLT1 near synapses diffuse orders of  
409 magnitude slower than all transporters on average (Murphy-Royal et al., 2015; Al  
410 Awabdh et al., 2016). Thus, the membrane-intracellular compartment exchange, rather  
411 than lateral diffusion, could be a preferred mechanism of the transporter turnover near  
412 synapses. Indeed, it has been estimated that small excitatory synapses release  $\sim 3000$   
413 glutamate molecules per vesicle (Savtchenko et al., 2013) and that  $10,000\text{-}15,000$   
414 GLT1 molecules are present within  $1\ \mu\text{m}^3$  of CA1 hippocampal neuropil (Lehre and  
415 Danbolt, 1998). Therefore, a rapid burst of several single-vesicle release events, or  
416 repeated multi-vesicular release, could lead to a relatively high occupancy, if not

417 saturation, of immobile GLT1 within the 1  $\mu\text{m}^3$  perisynaptic volume. The latter  
418 highlights the importance of reliable local resupply of GLT1, arguably through  
419 membrane turnover.

420 The present method has its own limitations. Similar to the QD approach, or any other  
421 live molecular tagging method, it is not technically feasible to verify fully that the  
422 labelled (or mutated) molecules have exactly the same dynamic properties as their  
423 native counterparts. Nonetheless, it is reassuring that the average lateral mobility of  
424 GLT1-SEP found here was similar to that estimated using QDs (Murphy-Royal et al.,  
425 2015), despite two very different modes of interference with the molecular structure.

426 The potential importance of high GLT1 diffusivity for regulating the waveform of  
427 excitatory synaptic currents was suggested earlier (Murphy-Royal et al., 2015). This  
428 might indeed be the case for large synapses, with multiple release sites (DiGregorio et  
429 al., 2002), that are prevalent in cultures or incubated slices. At small central synapses  
430 in situ, however, the kinetics of individual AMPA currents should not depend on  
431 glutamate buffering outside the synaptic cleft (Zheng et al., 2008; Savtchenko et al.,  
432 2013). Nonetheless, intense glutamatergic activity can boost glutamate escape from  
433 the cleft (Lozovaya et al., 1999), in which case lateral movement of astroglial  
434 transporters could indeed contribute to the efficiency of uptake.

435 Our results should provide critical real-time turnover data complementing the well-  
436 explored cellular machinery of GLT1 exocytosis and recycling in the plasma  
437 membrane (Gonzalez et al., 2007; Garcia-Tardon et al., 2012; Martinez-Villarreal et  
438 al., 2012; Piniella et al., 2018). At the same time, mechanisms that control lateral  
439 diffusion of GLT1 on the astroglial surface are only beginning to transpire. Two  
440 previous studies detected a diffusion-facilitating role of glutamate, which was either  
441 applied exogenously or released through intense neuronal network activity (Murphy-  
442 Royal et al., 2015; Al Awabdh et al., 2016), suggesting an adaptive function of GLT1  
443 mobility. Our results confirm these observations, but also provide further important  
444 functional associations between the expected sources of molecular signalling in the  
445 brain and GLT1 mobility. We found that the deletion of the C-terminus, or the blockade  
446 of glutamate receptors, intracellular  $\text{Ca}^{2+}$  buffering, or the suppression of the calcium  
447 and calmodulin-dependent phosphatase calcineurin made the GLT1 membrane  
448 mobility irresponsive to glutamate. This is in line with previous studies which have  
449 shown that blocking kinase activity promotes glutamate uptake (Adolph et al., 2007; Li

450 et al., 2015): lateral mobility might be one of the mechanisms assisting this process.  
451 Although regulation of GLT1 by calcineurin has previously been shown on the  
452 transcriptional level (Sompol et al., 2017), calcineurin is also known to directly  
453 dephosphorylate membrane proteins such as connexin-43 (Tence et al., 2012). At the  
454 same time, ATP application (which triggers prominent  $\text{Ca}^{2+}$ -dependent cascades in  
455 astrocytes) had no effect on GLT1 mobility. We have thus identified several molecular  
456 signalling cascades that might provide important clues to the possible regulatory  
457 intervention in brain pathologies associated with malfunctioning astroglial glutamate  
458 uptake (Fontana, 2015; Peterson and Binder, 2019).

459



## 460 MATERIALS AND METHODS

### 461 DNA constructs

462 cDNA of rat GLT1, cloned by Baruch Kanner group (Pines et al., 1992) under CMV  
463 promoter was a generous gift from Michael Robinson. Superecliptic pH-luorin (SEP)  
464 was introduced into second intracellular loop of GLT1 using standard cloning  
465 techniques. First, GLT1 sequence was mutated with QuikChange II Site-Directed  
466 Mutagenesis Kit [Agilent] using the following pair of primers:  
467 GTTCTGGTGGCACCTACGCGTCCATCCGAGGAG and  
468 CTCCTCGGATGGACGCGTAGGTGCCACCAGAAC in order to introduce MluI  
469 restriction site. Subsequently, SEP was amplified using pair of primers:  
470 CCGGACGCGTCTGGTTCCTCGTGGATCCGGAGGAATGAGTAAAGGAGAAGAAGT  
471 TTTCAC and  
472 CCGGACGCGTTCAGAAAGTGAACCAGATCCTCCTTTGTATAGTTCATCCATGCC  
473 ATG, which introduced linkers and enabled subcloning SEP into MluI restriction site.  
474 Resulting GLT1-SEP was subcloned into pZac2.1 gfaABC1D-tdTomato (Addgene  
475 Plasmid #44332) (Shigetomi et al., 2013) using BmtI and XbaI sites in order to be  
476 expressed under glia-specific gfaABC<sub>1</sub>D promoter. GLT1 $\Delta$ C-SEP was generated  
477 using following pair of primers: CCGATCTCGAGATGGCATCAACCGAGGGTG and  
478 CCGATGGTACCCTAGACACACTGATTAGAGTTGCTTTC which introduces “amber”  
479 stop codon after Val537 in GLT1 sequence. GLT1 $\Delta$ C-SEP was then cloned to plasmid  
480 pZac2.1gfaABC1D\_MCS which was generated by replacing tdTomato in pZac2.1  
481 gfaABC1D-tdTomato with hybridized pair of oligonucleotides:  
482 AATTCACCGGTGGCGCGCCGGATCCTGTACAACGCGTGATATCGGTACCCATAT  
483 GCCGCGGACTAGTT and  
484 CTAGAACTAGTCCGCGGCATATGGGTACCGATATCACGCGTTGTACAGGATCCG  
485 GCGCGCCACCGGTG cloned into EcoRI and XbaI sites. eGFP-GLT1 was generated  
486 by amplification of GFP with the following pair of primers:  
487 CTATAGGCTAGCATGGTGAGCAAGGGCG and  
488 CGTAACTCGAGGAATTCGCCAGAACCAGCAGCAGCGGAGCCAGCGGATCCCTTGATC  
489 AGCTCGTCCATG which introduced linker at 3' end of GFP and enabled for it using  
490 BmtI and XhoI sites at 5' end of GLT1 in pCMV\_GLT1 plasmid. Resulting eGFP-GLT1  
491 was subcloned into pZac2.1gfaABC1D\_MCS using BmtI and XbaI restriction sites.  
492 pDisplay-SEP was generated by subcloning SEP, amplified with a pair of primers:  
493 CCGCGAAGATCTATGAGTAAAGGAGAAGAAGTTCAC and  
494 GGCAGTCGACCTGCAGCCGCGGCCGTTTGTATAGTTCATCCATGCCATG into  
495 pDisplay-mSA-EGFP-TM (Addgene plasmid #39863) (Lim et al., 2013) using BglII and  
496 Sall restriction sites.

### 497 Cell cultures

498 HEK 293T (Lenti-X 293T subclone, TaKaRa) were maintained in DMEM, high glucose,  
499 GlutaMAX (Thermo Fisher Scientific) supplemented with 10% Fetal Bovine Serum  
500 (Thermo Fisher Scientific). For transfection and patch-clamp experiments cells were  
501 plated at density 25,000 cells per 13-mm-diameter coverslip (Assistent, Germany)

502 coated with poly-L-Lysine (Sigma-Aldrich). Cells were co-transfected with plasmids  
503 coding GLT1 or GLT1-SEP under CMV promoter together with mRFP1 under  $\beta$ -actin  
504 promoter in a 2:1 ratio using Lipofectamine 2000 (Thermo Fisher Scientific) according  
505 to manufacturer instructions. Transfected cells were used for patch clamp experiments  
506 the next day.

## 507 **Electrophysiology**

508 Patch clamp recordings were made from transfected HEK cells. Coverslips with cells  
509 were perfused with extracellular solution containing 125 mM NaCl, 2.5 mM KCl, 2 mM  
510  $\text{CaCl}_2$ , 1.3 mM  $\text{MgSO}_4$ , 26 mM  $\text{NaHCO}_3$ , 1.25 mM  $\text{NaH}_2\text{PO}_4$ , 12 mM D-glucose,  
511 bubbled with 95:5  $\text{O}_2/\text{CO}_2$  (pH 7.4). Patch pipettes were pulled to resistance of 4–5  
512 M $\Omega$  when filled with the intracellular solution containing 120 mM CsCl, 8 mM NaCl,  
513 10 mM HEPES, 0.2 mM  $\text{MgCl}_2$ , 2 mM EGTA, 2 mM MgATP, 0.3 mM  $\text{Na}_3\text{GTP}$  (pH  
514 7.3). Cells were voltage-clamped at  $-70$  mV, recordings were performed at 33°C–  
515 35°C and signals digitized at 10 kHz. For glutamate application, we used a  $\theta$ -glass  
516 pipette pulled out to an  $\sim 200$   $\mu\text{m}$  tip diameter, as described and illustrated earlier  
517 (Sylantsev and Rusakov, 2013). Briefly, a thin capillary was inserted into each  $\theta$ -glass  
518 channel, connected to the two-channel PDES-2DX-LA pneumatic microejector (npi  
519 electronic GmbH), with pressure adjusted using compressed nitrogen. The  $\theta$ -glass  
520 pipette was attached to a Bender piezoelectric actuator (PL127.11, Physik  
521 Instrumente) mounted on a micro-electrode holder held in a precision  
522 micromanipulator with remote control (Scientifica Ltd). Square electric pulses of  
523 chosen duration were applied to the actuator using a constant-voltage stimulus  
524 isolator (DS2, Digitimer), which moved the  $\theta$ -glass pipette so that the tested cell was  
525 exposed to either channels, with the channel boundary monitored in the DIC channel  
526 (Sylantsev and Rusakov, 2013).

## 527 **Primary dissociated culture**

528 Dissociated hippocampal cultures from P0 (postnatal day 0) Sprague-Dawley rats  
529 were prepared in full compliance with the national guideline and the European  
530 Communities Council Directive of November 1986, and the European Directive  
531 2010/63/EU on the Protection of Animals used for Scientific Purposes. Brains were  
532 removed and hippocampi were isolated on ice in dissociation medium - DM (81.8 mM  
533  $\text{Na}_2\text{SO}_4$ , 30 mM  $\text{K}_2\text{SO}_4$ , 5.8 mM  $\text{MgCl}_2$ , 0.25 mM  $\text{CaCl}_2$ , 1 mM HEPES pH 7.4, 20 mM  
534 glucose, 1 mM kynureic acid, 0.001% Phenol Red), hippocampi were later incubated  
535 twice for 15 minutes at 37°C with 100 units of papain (Worthington, NY) in DM and  
536 rinsed three times in DM and subsequently three times in plating medium (MEM, 10%  
537 fetal bovine serum (FBS) and 1% penicillin-streptomycin; Thermo Fisher Scientific).  
538 Hippocampi were triturated in plating medium until no clumps were visible and cells  
539 were diluted 1:10 in OptiMEM (Thermo Fisher Scientific), centrifuged for 10 minutes at  
540 room temperature, at 200 x g. The resulting cell pellet was suspended in plating  
541 medium, cells were counted in 1:1 dilution of 0.4% Trypan Blue solution (Thermo  
542 Fisher Scientific) and plated at density 75,000 cells per 13-mm-diameter coverslip  
543 (Assistent, Germany) coated with 1 mg/ml poly-DL-lysine (Sigma-Aldrich, P9011) and

544 2.5 µg/ml laminin (Sigma-Aldrich, L2020). Three hours after plating medium was  
545 exchanged for maintenance medium (Neurobasal-A without Phenol Red, 2% B-27  
546 supplement, 1% penicillin-streptomycin, 0.5 mM GlutaMAX, 25 µM β-mercaptoethanol;  
547 ThermoFisher Scientific) and cells were kept at 37°C, under a humidified 5% CO<sub>2</sub>  
548 atmosphere. Cells were transfected with plasmids using Lipofectamine 3000 (Thermo  
549 Fisher Scientific) at 7-10 days in vitro (DIV). Lipofectamine – DNA complexes were  
550 prepared according to manufacturer's instructions and were incubated with cells for 1  
551 h in the incubator, in fresh transfection medium (MEM without Phenol Red, 2% B27  
552 supplement, 1mM pyruvate, 0.5 mM GlutaMAX, 25 µM β-mercaptoethanol; Thermo  
553 Fisher Scientific). After transfection conditioned maintenance medium was returned to  
554 cells. All experiments were performed at 14–19 DIV.

### 555 **Western blot in HEK cells**

556 HEK 293T were co-transfected with plasmids coding GLT1 or GLT1-SEP under CMV  
557 promoter together with mRFP1 under β-actin promoter in a 2:1 ratio using  
558 Lipofectamine 2000 (Thermo Fisher Scientific), in accord with manufacturer  
559 instructions. After 24h cells were lysed using 1x Leammli solution, and the samples  
560 were loaded on 10% polyacrylamide gels. The samples were electro-transferred onto  
561 polyvinylidene difluoride membranes (Immobilon-P, Millipore), which were blocked 2 h  
562 at room temperature with 10% nonfat milk in Tris-buffered saline with 0.1% Tween 20  
563 (TBS-T). After blocking, the membranes were incubated at 4°C overnight with the  
564 following antibodies: 1:1000 anti-GLT1(ex) (Synaptic Systems # 250 203;  
565 AB11042312), diluted in 5% non-fat milk in TBS-T. The membranes were next  
566 incubated for 2h at room temperature (RT) with the peroxidase-labelled secondary  
567 antibody (Goat Anti-Rabbit IgG Antibody; Vector Laboratories, #PI-1000;  
568 AB\_2336198) diluted 1:10,000 in 5% non-fat milk in TBS-T. After washing, peroxidase  
569 activity was visualized with the ECL Prime reagent (GE Healthcare #RPN2232). The  
570 membranes were next stripped for 1h at 50°C with a buffer containing: 62.5 mM Tris-  
571 Cl pH6.8, 2% SDS and 120 mM β-mercaptoethanol, washed three times with TBS-T,  
572 blocked for 2h at RT with 10% non-fat milk in TBS-T and probed with anti-alpha-  
573 Tubulin antibody (Sigma-Aldrich #T9026; AB\_477593) diluted 1:5,000 in 5% non-fat  
574 milk. The membranes were washed three times with TBS-T and incubated with  
575 peroxidase-labelled secondary antibody (Horse Anti-Mouse IgG Antibody, Vector  
576 Laboratories, #PI-2000; AB\_2336177) diluted 1:10,000 in 5% non-fat milk. After  
577 washing, peroxidase activity was visualized with the ECL Prime reagent.

### 578 **Immunostaining in HEK cells**

579 HEK 293T were co-transfected with the plasmids coding GLT1 or GLT1-SEP under  
580 CMV promoter, together with mRFP1 under β-actin promoter, in a 2:1 ratio using  
581 Lipofectamine 2000 (Thermo Fisher Scientific), in accord with manufacturer  
582 instructions. After 24h the cells were fixed using 37°C pre-warmed 4%  
583 paraformaldehyde in PBS for 10 minutes at 37°C, were washed trice in PBS,  
584 permeabilised in 0.1% Triton X-100 for 10 minutes and blocked with 3% BSA and 10%  
585 Normal Goat Serum in PBS for 1 hour at RT. Afterwards, cells were incubated with the

586 primary antibody (see below) in 1.5% BSA and 5% Normal Goat Serum in PBS  
587 overnight at 4°C, washed trice with PBS, incubated with the secondary antibody (see  
588 below) in 1.5% BSA and 5% Normal Goat Serum in PBS for 2 hours, washed trice with  
589 PBS. The cells were mounted using Fluoromount-G™ Mounting Medium (Thermo  
590 Fisher Scientific #00-4958-02) and stored at 4°C until imaging.

591 The primary antibodies used were: glial glutamate transporter GLT1 (guinea pig,  
592 polyclonal, synthetic peptide from the C-terminus of rat GLT1, Merck, AB1783,  
593 AB\_90949, dilution 1:1,000), GFP (chicken, polyclonal, GFP directly from Aequorea  
594 Victoria, Thermo Fisher Scientific, A10262, AB\_2534023, dilution 1:1,000). The  
595 secondary antibodies: anti-chicken IgY (goat, Alexa Fluor 488, Thermo Fisher  
596 Scientific, A32931, dilution: 1:1,000), anti-guinea pig IgG (goat, Alexa Fluor 647,  
597 Thermo Fisher Scientific, A-21450, dilution: 1:1,000). Images were recorded with Zeiss  
598 780 confocal microscope using 40X/1.4 NA Oil Plan-Apochromat objective. As HEK  
599 cells do not express endogenous GLT1, only the cells which transfected with  
600 mRFP1 were analysed for GLT1 expression.

### 601 **Organotypic hippocampal culture**

602 Transverse hippocampal organotypic cultures were prepared according to Stoppini  
603 and colleagues (Stoppini et al., 1991) with some modifications. P8 Sprague-Dawley  
604 rats were sacrificed in full compliance with the national guideline and the European  
605 Communities Council Directive of November 1986, and the European Directive  
606 2010/63/EU on the Protection of Animals used for Scientific Purposes. Hippocampi  
607 were dissected in ice-cold Gey's Balanced Salt Solution (Merck) supplemented with 28  
608 mM glucose, 1 mM Kynureic acid and 10 mM MgCl<sub>2</sub>, and 350 µm hippocampal slices  
609 were cut using Mcllwain tissue chopper. Slices were cultured on 0.4 µm Millicell  
610 membrane inserts (Merck) in Minimum Essential Medium (MP Biomedicals)  
611 supplemented with 25% Hank's Balanced Salt Solution (MP Biomedicals), 25% horse  
612 serum, 1% Penicillin-Streptomycin, 1 mM GlutaMax (all Thermo Fisher Scientific), and  
613 28 mM Glucose (Sigma-Aldrich). Medium was changed 3 times per week. After 4 DIV,  
614 cultures were transfected with plasmids using a biolistic method (Helios Gene Gun,  
615 Bio-Rad). To obtain sparse astrocyte labelling we used 1 µm gold particles (Bio-Rad)  
616 and followed a standard protocol (Benediktsson et al., 2005) for preparation of gene  
617 gun bullets. Slices were shot at 160 PSI Helium pressure using modified gene gun  
618 barrel, in accord with accepted routines (Woods and Zito, 2008), where diffuser screen  
619 were replaced with stainless steel wire mesh (180 mesh per inch, 36% open area;  
620 Advent Research Materials Ltd.). Slices were used for experiments 4-10 days after  
621 transfection.

### 622 **Immunostaining in cultures**

623 Cultures transfected with GLT1-SEP or GLT1ΔC-SEP were fixed using 37°C pre-  
624 warmed 4% paraformaldehyde in PBS for 10 minutes at 37°C, washed trice in PBS,  
625 cell-permeabilised in 0.1% Triton X-100 for 10 minutes and blocked with 3% BSA and  
626 10% Normal Goat Serum in PBS for 1 hour at RT. Afterwards, the cultured were

627 incubated with the primary antibody (see below) in 1.5% BSA and 5% Normal Goat  
628 Serum in PBS overnight at 4°C, washed trice with PBS, incubated with the secondary  
629 antibody (see below) in 1.5% BSA and 5% Normal Goat Serum in PBS for 2h, and  
630 washed trice with PBS. The cultures were mounted using Fluoromount-G™ Mounting  
631 Medium (Thermo Fisher Scientific #00-4958-02) and stored at 4°C until imaging.

632 The primary antibodies used were: glial glutamate transporter GLT1 (guinea pig,  
633 polyclonal, synthetic peptide from the C-terminus of rat GLT1, Merck, AB1783,  
634 AB\_90949, dilution 1:1,000), GFP (chicken, polyclonal, GFP directly from *Aequorea*  
635 *Victoria*, Thermo Fisher Scientific, A10262, AB\_2534023, dilution 1:1,000). Secondary  
636 antibodies: anti-chicken IgY (goat, Alexa Fluor 488, Thermo Fisher Scientific, A32931,  
637 dilution: 1:1,000), anti-guinea pig IgG (goat, Alexa Fluor 647, Thermo Fisher Scientific,  
638 A-21450, dilution: 1:1,000). Images were recorded with Zeiss 780 confocal microscope  
639 using 40X/1.4 NA Oil Plan-Apochromat objective. The analyses were carried out in Fiji  
640 (NIH) using in-house written custom macros. The GLT1 fluorescence levels were  
641 measured in transfected cells versus non-transfected using the mask of GFP  
642 fluorescence for separation between the two groups. The mean fluorescence intensity  
643 were measured and compared in situ, for transfected and non-transfected, for each  
644 individual ROI image.

#### 645 **Imaging and FRAP**

646 Imaging was performed using an Olympus FV1000 system under Olympus XLPlan  
647 N25 x water immersion objective (NA 1.05). Imaging system was linked to two mode-  
648 locked, femtosecond-pulse Ti:Sapphire lasers (MaiTai from SpectraPhysics-Newport  
649 and Chameleon from Coherent), first one for imaging, was set at a wavelength of 910  
650 nm and the other was for bleaching set on 690 nm, each of the lasers was connected  
651 to the microscope via an independent scan head. 690 nm for bleaching was selected  
652 based on the 2-P excitation spectrum for GFP (Drobizhev et al., 2011). The imaging  
653 laser power was kept below 4 mW under the objective at all times to minimize  
654 phototoxic damage, a power range validated by us previously in similar settings  
655 (Jensen et al., 2019). Bleaching laser power was kept around 10 mW. Dissociated  
656 mixed cultures were imaged in extracellular solution containing: 125 mM NaCl, 2.5 mM  
657 KCl, 30 mM Glucose, 25 mM HEPES, 2 mM CaCl<sub>2</sub> and 1.3 mM MgSO<sub>4</sub>; pH 7.4, at 32-  
658 34°C. In puffing experiments, pH 5.5 extracellular solution contained: 125 mM NaCl,  
659 2.5 mM KCl, 30 mM Glucose, 25 mM MES, 2 mM CaCl<sub>2</sub> and 1.3 mM MgSO<sub>4</sub>,  
660 Extracellular solution with 50mM NH<sub>4</sub>Cl contained: 50 mM NH<sub>4</sub>Cl, 75 mM NaCl, 2.5  
661 mM KCl, 30 mM Glucose, 25 mM HEPES, 2 mM CaCl<sub>2</sub> and 1.3 mM MgSO<sub>4</sub>, pH 7.4.

662 Organotypic cultures were imaged in artificial cerebrospinal fluid (aCSF) containing:  
663 125 mM NaCl, 2.5 mM KCl, 2 mM CaCl<sub>2</sub>, 1.3 mM MgSO<sub>4</sub>, 26 mM NaHCO<sub>3</sub>, 1.25 mM  
664 NaH<sub>2</sub>PO<sub>4</sub>, 20 mM D-glucose, 0.2 mM Trolox, bubbled with 95:5 O<sub>2</sub>/CO<sub>2</sub> (pH 7.4) at 32-  
665 34°C.

666 FRAP experiments were performed using 22 x zoom at 256 x 256 numerical  
667 resolution, resulting in a ~0.09 µm pixel size. Frame size was kept constant: 138 x 80

668 pixels, giving 148.32 ms per frame (unidirectional scanning, 4.0  $\mu$ s pixel dwell time).  
669 The small ( $\sim$ 1.6  $\mu$ m wide) FRAP ROIs were selected in a quasi-random fashion. As in  
670 the hippocampal area CA1 the mean inter-synaptic distance is  $\sim$ 0.5  $\mu$ m (Rusakov and  
671 Kullmann, 1998), each ROIs was equally likely to include 1-3 PSDs and the  
672 perisynaptic areas, thus providing a relatively homogenous sampling. The bleached  
673 ROI region was thus kept constant – a 18-pixels diameter circle (2.06  $\mu$ m<sup>2</sup>) scanned  
674 with second laser using tornado mode, resulting in fast bleaching time – 46 ms. In  
675 some experiments, drugs (1 mM Glutamate or 100  $\mu$ M ATP) were puffed for 250 ms  
676 just before the bleaching using Pneumatic PicoPump (World Precision Instruments).  
677 Imaging, bleaching and puffing were synchronized using Axon Digidata digitizer  
678 (Molecular Devices).

679 For whole cell FRAP (only in dissociated culture) 512 x 512 pixel frames were imaged  
680 every 1.644 s. Bleached region – 398-pixels diameter circle was scanned with second  
681 laser using tornado mode resulting in fast bleaching time – 2.00 s. In order to image  
682 and bleach as big astrocyte surface as possible, we used 2 to 5 x zoom resulting in  
683 corresponding pixel size 0.497  $\mu$ m to 0.198  $\mu$ m. Pixel size was taken into account for  
684 data analysis and calculations.

685 In some FRAP experiments (see Results) we used the following drugs in the bath  
686 solution: TTX (1  $\mu$ M, Tocris), MPEP (1  $\mu$ M, Tocris), NBQX (10  $\mu$ M, Tocris), LY 341495  
687 (30 nM, Tocris), YM (300 nM, Tocris), Bicuculine (10  $\mu$ M, Sigma-Aldrich), 4-AP (4-  
688 Aminopyridine, 500  $\mu$ M, Sigma-Aldrich), FK-506 (1  $\mu$ M, Sigma-Aldrich), Staurosporine  
689 (100 nM, Cell Signaling Techn.).

690

## 691 **Super-resolution microscopy**

692 We used the single-molecule localization microscopy (SMLM) technique direct  
693 stochastic optical reconstruction microscopy (dSTORM) (van de Linde et al., 2011;  
694 Endesfelder and Heilemann, 2015) as described previously (Heller et al., 2017; Heller  
695 and Rusakov, 2019; Heller et al., 2020). Naïve dissociated hippocampal cultures and  
696 cultures expressing either GLT1-SEP or GLT1 $\Delta$ C-SEP were fixed using 37°C pre-  
697 warmed 4% paraformaldehyde in PEM buffer (80 mM PIPES pH 6.8, 5 mM EGTA, 2  
698 mM MgCl<sub>2</sub>) (Leyton-Puig et al., 2016; Pereira et al., 2019) for 10 minutes at 37°C.  
699 Then, cells were washed thrice in PBS, incubated in 0.1% NaBH<sub>4</sub> in PBS for 7  
700 minutes, washed thrice with PBS and incubated in 10 mM CuSO<sub>4</sub> in 50 mM NH<sub>4</sub>Cl,  
701 final pH = 5 for 10 minutes. Cells were washed thrice with water quickly and once with  
702 PBS. Cells were then permeabilised and blocked with PBS-S (0.2% saponin in PBS)  
703 supplemented with 3% BSA for 1 hour. Afterwards, cells were incubated with primary  
704 antibody (see below) in PBS-S overnight at 4°C, washed thrice with PBS-S, incubated  
705 with secondary antibody (see below) in PBS-S for 2 hours, washed twice with PBS-S  
706 and twice with PBS. Lastly, cells were post-fixed with 4% paraformaldehyde in PBS,  
707 washed thrice with PBS and stored at 4°C until being prepared for imaging.

708 Primary antibodies used: post-synaptic protein PSD-95 (mouse, 6G6-1C9,  
709 recombinant rat PSD-95, Novus Biologicals, NB110-61643, AB\_965165, dilution  
710 1:500), glial glutamate transporter GLT1 (guinea pig, polyclonal, synthetic peptide from  
711 the C-terminus of rat GLT1, Merck, AB1783, AB\_90949, dilution 1:1,000), GFP  
712 (chicken, polyclonal, GFP directly from *Aequorea Victoria*, Thermo Fisher Scientific,  
713 A10262, AB\_2534023, dilution 1:1,000).

714 Secondary antibodies used: anti-mouse IgG (donkey, CF568-conjugated, Biotium,  
715 20105, AB\_10557030, dilution 1:500), anti-chicken IgY (goat, Alexa647-conjugated,  
716 Thermo Fisher Scientific, A21449, AB\_1500594, dilution: 1:1,000), anti-guinea pig IgG  
717 (donkey, Alexa647-conjugated, Jackson ImmunoResearch Labs, 706-606-148,  
718 AB\_2340477, dilution: 1:1,000).

719 Images were recorded with a Vutara 350 microscope (Bruker) in photo-switching  
720 buffer containing 100 mM cysteamine and oxygen scavengers (glucose oxidase and  
721 catalase) (Metcalf et al., 2013). Images were recorded with frame rate of 33 Hz (561  
722 nm for CF568) or 66 Hz (640 nm for Alexa647). Total number of frames acquired per  
723 channel ranged from 3,000 to 20,000. Data were analysed using the Vutara SRX  
724 software (version 6.02.05). Fiducial markers (100 nm TetraSpeck microspheres,  
725 T7279, Thermo Fisher Scientific) were used for drift correction.

## 726 **Cluster and Nearest-neighbour analysis**

727 In dSTORM maps, clusters of PSD95 were identified using DBScan, a well-  
728 established density-based clustering algorithm (Ester et al., 1996), with a minimum of  
729 50 particles per cluster and a maximum particle distance of 100 nm; the latter  
730 parameters correspond to 250-300 nm wide PSD5 clusters which are consistent with  
731 the typical PSD size at common central synapses (Chen et al., 2008). The total 2D  
732 area for analysis for each GLT1 variant was  $\sim 360 \mu\text{m}^2$ , the cut-off distance for  
733 nearest-neighbour analyses was 500 nm, sampled within the 1  $\mu\text{m}$  wide ROIs selected  
734 arbitrarily. Overall, the WT GLT1 samples contained 876904 molecular positions and  
735 22887 nearest-neighbour distance measurements, GLT1-SEP samples contained  
736 715977 positions and 5021 distances, GLT1 $\Delta$ C-SEP samples contained 457221  
737 positions and 7193 distances.

738 The distribution of nearest-neighbour distances  $D(r)$  between PSD95 clusters and  
739 GLT1 molecular species (and also among GLT1 molecular species) was calculated as  
740 the occurrence of distances  $r$ , with a 5 nm or 10 nm binning step, and normalised to  
741 the overall number of registered events. To assess non-uniformity of the experimental  
742 distribution pattern  $D(r)$  was compared to the theoretical  $D(r)$  of a 2D Poisson point  
743 process (evenly random scatter) of the same surface density  $\lambda$ , in the form  
744  $D(r) = 1 - \exp(-\lambda\pi r^2)$  (Stoyan, 2006).

745

## 746 **FRAP data analysis**

747 Raw images were analysed using ImageJ. Mean fluorescence intensity was calculated  
748 for manually selected ROIs: Background - manually selected background ROI outside  
749 of transfected cell (FBKG), reference ROI which was manually outlined transfected  
750 cell in the imaged frame (FREF). For each frame mean fluorescence intensity of  
751 bleached ROI (FBL) was normalized according to the formula:  $F_{NOR} = (F_{BL} -$   
752  $F_{BKG}) / (F_{REF} - F_{BKG})$ . Normalized fluorescence value at the frame after the  
753 bleaching pulse (close to the background value) was subtracted from all values in data  
754 set. Finally, resulting fluorescence values were normalized to 40 frames before  
755 bleaching.

756 For the whole-cell bleaching experiments we performed similar analysis however for  
757 each cell we have measured mean fluorescence in manually selected 3 ROIs (FROI)  
758 defined as ~10  $\mu\text{m}$  diameter circle placed outside of the cell soma. Additionally for  
759 each analysed data set we measured mean fluorescence in manually selected  
760 background ROI (FBKG) – outside of transfected cell and in reference ROI (FREF)  
761 which was manually outlined transfected cell outside of bleached region. We  
762 performed the same normalization for each specific ROI as described above. The  
763 kinetic analyses of membrane turnover and FRAP traces were carried out as detailed  
764 in Fig.s S1-S2. The FRAP time course  $C_{mem}^f = RC_{in} (e^{-k_b t} - e^{-k_t t})$  (notations in Figure 1  
765 -figure supplement 1-S2) was fitted using the non-linear fitting routines ExpGroDec  
766 (exponent fitting) in Origin (OriginLab).

767 To evaluate lateral diffusivity from the spot-FRAP kinetics, we used the well-  
768 established Soumpasis method for circular ROIs (Soumpasis, 1983; Kang et al.,  
769 2009), in which the fluorescence time course is fitted with the equation

770 
$$F(t) = C_{mob} \exp\left(-\frac{2\tau_D}{t}\right) \cdot \left( I_0\left(\frac{2\tau_D}{t}\right) + I_1\left(\frac{2\tau_D}{t}\right) \right)$$
 where  $C_{mob}$  is the mobile fraction,

771  $\tau_D = \frac{w^2}{4D}$ ,  $w$  is ROI radius,  $D$  is diffusion coefficient, and  $I_0$  and  $I_1$  are modified Bessel  
772 functions of the first kind; this fitting has only two free parameters,  $C_{mob}$  and  $D$ . The  
773 fitting was carried out using Soumpasis in the Origin software (OriginLab). The  
774 average diffusivity  $D^*$  was therefore calculated as  $D^* = C_{mob} \cdot D$ .

775 Statistical inference was calculated using Origin's Hypothesis Testing from individual  
776 ROIs as statistical units (2-4 per cell): routine two-way ANOVA tests indicated no  
777 significant influence of the cell identity factor on the effects of experimental  
778 manipulations under study.

779



780 **ACKNOWLEDGEMENTS**

781 The study was supported by the Wellcome Trust Principal Fellowship  
782 (212251\_Z\_18\_Z), ERC Advanced Grant (323113) and European Commission  
783 NEUROTWIN grant (857562), to DAR.

784

785 **COMPETING INTERESTS**

786 The authors declare no competing interests

787

788 **REFERENCES**

- 789 Adolph O, Koster S, Rath M, Georgieff M, Weigt HU, Engele J, Senftleben U, Fohr KJ.  
790 2007. Rapid increase of glial glutamate uptake via blockade of the protein kinase  
791 A pathway. *Glia* **55**: 1699-1707.
- 792 Al Awabdh S, Gupta-Agarwal S, Sheehan DF, Muir J, Norkett R, Twelvetrees AE,  
793 Griffin LD, Kittler JT. 2016. Neuronal activity mediated regulation of glutamate  
794 transporter GLT-1 surface diffusion in rat astrocytes in dissociated and slice  
795 cultures. *Glia* **64**: 1252-1264.
- 796 Arnth-Jensen N, Jabaudon D, Scanziani M. 2002. Cooperation between independent  
797 hippocampal synapses is controlled by glutamate uptake. *Nature Neuroscience* **5**:  
798 325-331.
- 799 Benediktsson AM, Schachtele SJ, Green SH, Dailey ME. 2005. Ballistic labeling and  
800 dynamic imaging of astrocytes in organotypic hippocampal slice cultures. *J*  
801 *Neurosci Methods* **141**: 41-53.
- 802 Bergles DE, Jahr CE. 1998. Glial contribution to glutamate uptake at Schaffer  
803 collateral- commissural synapses in the hippocampus. *Journal of Neuroscience*  
804 **18**: 7709-7716.
- 805 Bergles DE, Tzingounis AV, Jahr CE. 2002. Comparison of coupled and uncoupled  
806 currents during glutamate uptake by GLT-1 transporters. *J Neurosci* **22**: 10153-  
807 10162.
- 808 Chen X, Winters C, Azzam R, Li X, Galbraith JA, Leapman RD, Reese TS. 2008.  
809 Organization of the core structure of the postsynaptic density. *Proc Natl Acad Sci*  
810 *U S A* **105**: 4453-4458.
- 811 Danbolt NC. 2001. Glutamate uptake. *Progress in Neurobiology* **65**: 1-105.
- 812 Diamond JS, Jahr CE. 2000. Synaptically released glutamate does not overwhelm  
813 transporters on hippocampal astrocytes during high-frequency stimulation. *J*  
814 *Neurophysiol* **83**: 2835-2843.
- 815 DiGregorio DA, Nusser Z, Silver RA. 2002. Spillover of glutamate onto synaptic AMPA  
816 receptors enhances fast transmission at a cerebellar synapse. *Neuron* **35**: 521-  
817 533.
- 818 Drobizhev M, Makarov NS, Tillo SE, Hughes TE, Rebane A. 2011. Two-photon  
819 absorption properties of fluorescent proteins. *Nat Methods* **8**: 393-399.
- 820 Endesfelder U, Heilemann M. 2015. Direct stochastic optical reconstruction  
821 microscopy (dSTORM). *Methods Mol Biol* **1251**: 263-276.

822 Ester M, Kriegel HP, Sander J, Xu X (1996) A density-based algorithm for discovering  
823 clusters in large spatial databases with noise. In: KDD'96: Proceedings of the  
824 Second International Conference on Knowledge Discovery and Data Mining, pp  
825 226-231. Portland, Oregon: AAAI Press.

826 Fontana AC. 2015. Current approaches to enhance glutamate transporter function and  
827 expression. *J Neurochem* **134**: 982-1007.

828 Foran E, Rosenblum L, Bogush A, Pasinelli P, Trotti D. 2014. Sumoylation of the  
829 astroglial glutamate transporter EAAT2 governs its intracellular  
830 compartmentalization. *Glia* **62**: 1241-1253.

831 Fournier KM, Gonzalez MI, Robinson MB. 2004. Rapid trafficking of the neuronal  
832 glutamate transporter, EAAC1 - Evidence for distinct trafficking pathways  
833 differentially regulated by protein kinase C and platelet-derived growth factor.  
834 *Journal of Biological Chemistry* **279**: 34505-34513.

835 Garcia-Tardon N, Gonzalez-Gonzalez IM, Martinez-Villarreal J, Fernandez-Sanchez  
836 E, Gimenez C, Zafra F. 2012. Protein kinase C (PKC)-promoted endocytosis of  
837 glutamate transporter GLT-1 requires ubiquitin ligase Nedd4-2-dependent  
838 ubiquitination but not phosphorylation. *J Biol Chem* **287**: 19177-19187.

839 Gibb SL, Boston-Howes W, Lavina ZS, Gustincich S, Brown RH, Jr., Pasinelli P, Trotti  
840 D. 2007. A caspase-3-cleaved fragment of the glial glutamate transporter EAAT2  
841 is sumoylated and targeted to promyelocytic leukemia nuclear bodies in mutant  
842 SOD1-linked amyotrophic lateral sclerosis. *J Biol Chem* **282**: 32480-32490.

843 Gonzalez-Gonzalez IM, Garcia-Tardon N, Gimenez C, Zafra F. 2008. PKC-dependent  
844 endocytosis of the GLT1 glutamate transporter depends on ubiquitylation of  
845 lysines located in a C-terminal cluster. *Glia* **56**: 963-974.

846 Gonzalez MI, Susarla BT, Fournier KM, Sheldon AL, Robinson MB. 2007. Constitutive  
847 endocytosis and recycling of the neuronal glutamate transporter, excitatory amino  
848 acid carrier 1. *J Neurochem* **103**: 1917-1931.

849 Heller JP, Rusakov DA. 2019. A Method to Visualize the Nanoscopic Morphology of  
850 Astrocytes In Vitro and In Situ. *Methods Mol Biol* **1938**: 69-84.

851 Heller JP, Michaluk P, Sugao K, Rusakov DA. 2017. Probing nano-organization of  
852 astroglia with multi-color super-resolution microscopy. *J Neurosci Res* **95**: 2159-  
853 2171.

854 Heller JP, Odii T, Zheng KY, Rusakov DA. 2020. Imaging tripartite synapses using  
855 super-resolution microscopy. *Methods* **174**: 81-90.

856 Henneberger C et al. 2020. LTP Induction Boosts Glutamate Spillover by Driving  
857 Withdrawal of Perisynaptic Astroglia. *Neuron* **108**: 919-936 e911.

858 Holmseth S, Scott HA, Real K, Lehre KP, Leergaard TB, Bjaalie JG, Danbolt NC.  
859 2009. The concentrations and distributions of three C-terminal variants of the  
860 GLT1 (EAAT2; slc1a2) glutamate transporter protein in rat brain tissue suggest  
861 differential regulation. *Neuroscience* **162**: 1055-1071.

862 Jensen TP, Zheng KY, Cole N, Marvin JS, Looger LL, Rusakov DA. 2019. Multiplex  
863 imaging relates quantal glutamate release to presynaptic Ca<sup>2+</sup> homeostasis at  
864 multiple synapses in situ. *Nature Communications* **10**: 1414.

865 Kalandadze A, Wu Y, Robinson MB. 2002. Protein kinase C activation decreases cell  
866 surface expression of the GLT-1 subtype of glutamate transporter. Requirement of  
867 a carboxyl-terminal domain and partial dependence on serine 486. *J Biol Chem*  
868 **277**: 45741-45750.

869 Kang M, Day CA, Drake K, Kenworthy AK, DiBenedetto E. 2009. A generalization of  
870 theory for two-dimensional fluorescence recovery after photobleaching applicable  
871 to confocal laser scanning microscopes. *Biophys J* **97**: 1501-1511.

872 Kopach O, Zheng KY, Rusakov DA. 2020. Optical monitoring of glutamate release at  
873 multiple synapses in situ detects changes following LTP induction. *Molecular Brain*  
874 **13**.

875 Kruyer A, Scofield MD, Wood D, Reissner KJ, Kalivas PW. 2019. Heroin Cue-Evoked  
876 Astrocytic Structural Plasticity at Nucleus Accumbens Synapses Inhibits Heroin  
877 Seeking. *Biological Psychiatry* **86**: 811-819.

878 Lee Y, Messing A, Su M, Brenner M. 2008. GFAP promoter elements required for  
879 region-specific and astrocyte-specific expression. *Glia* **56**: 481-493.

880 Lehre KP, Danbolt NC. 1998. The number of glutamate transporter subtype molecules  
881 at glutamatergic synapses: Chemical and stereological quantification in young  
882 adult rat brain. *Journal of Neuroscience* **18**: 8751-8757.

883 Leyton-Puig D, Kedziora KM, Isogai T, van den Broek B, Jalink K, Innocenti M. 2016.  
884 PFA fixation enables artifact-free super-resolution imaging of the actin  
885 cytoskeleton and associated proteins. *Biology Open* **5**: 1001-1009.

886 Li D, Herault K, Zylbersztejn K, Lauterbach MA, Guillon M, Oheim M, Ropert N. 2015.  
887 Astrocyte VAMP3 vesicles undergo Ca<sup>2+</sup> -independent cycling and modulate  
888 glutamate transporter trafficking. *J Physiol* **593**: 2807-2832.

889 Lim KH, Huang H, Pralle A, Park S. 2013. Stable, high-affinity streptavidin monomer  
890 for protein labeling and monovalent biotin detection. *Biotechnol Bioeng* **110**: 57-  
891 67.

892 Lozovaya NA, Kopanitsa MV, Boychuk YA, Krishtal OA. 1999. Enhancement of  
893 glutamate release uncovers spillover-mediated transmission by N-methyl-D-  
894 aspartate receptors in the rat hippocampus. *Neuroscience* **91**: 1321-1330.

895 Maragakis NJ, Rothstein JD. 2004. Glutamate transporters: animal models to  
896 neurologic disease. *Neurobiol Dis* **15**: 461-473.

897 Martinez-Villarreal J, Garcia Tardon N, Ibanez I, Gimenez C, Zafra F. 2012. Cell  
898 surface turnover of the glutamate transporter GLT-1 is mediated by  
899 ubiquitination/deubiquitination. *Glia* **60**: 1356-1365.

900 Metcalf DJ, Edwards R, Kumarswami N, Knight AE. 2013. Test Samples for  
901 Optimizing STORM Super-Resolution Microscopy. *Jove-Journal of Visualized*  
902 *Experiments*.

903 Moussawi K, Riegel A, Nair S, Kalivas PW. 2011. Extracellular glutamate: functional  
904 compartments operate in different concentration ranges. *Front Syst Neurosci* **5**:  
905 94.

906 Murphy-Royal C, Dupuis JP, Varela JA, Panatier A, Pinson B, Baufreton J, Groc L,  
907 Oliet SH. 2015. Surface diffusion of astrocytic glutamate transporters shapes  
908 synaptic transmission. *Nat Neurosci* **18**: 219-226.

909 Pereira PM, Albrecht D, Culley S, Jacobs C, Marsh M, Mercer J, Henriques R. 2019.  
910 Fix Your Membrane Receptor Imaging: Actin Cytoskeleton and CD4 Membrane  
911 Organization Disruption by Chemical Fixation. *Frontiers in Immunology* **10**.

912 Peterson AR, Binder DK. 2019. Post-translational Regulation of GLT-1 in Neurological  
913 Diseases and Its Potential as an Effective Therapeutic Target. *Front Mol Neurosci*  
914 **12**: 164.

915 Pines G, Danbolt NC, Bjoras M, Zhang YM, Bendahan A, Eide L, Koepsell H, Storm-  
916 Mathisen J, Seeberg E, Kanner BI. 1992. Cloning and expression of a rat brain L-  
917 glutamate transporter. *Nature* **360**: 464-467.

918 Piniella D, Martinez-Blanco E, Ibanez I, Bartolome-Martin D, Porlan E, Diez-Guerra J,  
919 Gimenez C, Zafra F. 2018. Identification of novel regulatory partners of the  
920 glutamate transporter GLT-1. *Glia* **66**: 2737-2755.

921 Porter JT, McCarthy KD. 1997. Astrocytic neurotransmitter receptors in situ and in  
922 vivo. *Prog Neurobiol* **51**: 439-455.

923 Rudolph F, Huttemeister J, da Silva Lopes K, Juttner R, Yu L, Bergmann N, Friedrich  
924 D, Preibisch S, Wagner E, Lehnart SE, Gregorio CC, Gotthardt M. 2019.  
925 Resolving titin's lifecycle and the spatial organization of protein turnover in mouse  
926 cardiomyocytes. *Proc Natl Acad Sci U S A* **116**: 25126-25136.

927 Rusakov DA, Kullmann DM. 1998. Extrasynaptic glutamate diffusion in the  
928 hippocampus: ultrastructural constraints, uptake, and receptor activation. *Journal*  
929 *of Neuroscience* **18**: 3158-3170.

930 Savtchenko LP, Sylantsev S, Rusakov DA. 2013. Central synapses release a  
931 resource-efficient amount of glutamate. *Nature Neuroscience* **16**: 10-U163.

932 Scimemi A, Fine A, Kullmann DM, Rusakov DA. 2004. NR2B-containing receptors  
933 mediate cross talk among hippocampal synapses. *Journal of Neuroscience* **24**:  
934 4767-4777.

935 Shigetomi E, Bushong EA, Haustein MD, Tong X, Jackson-Weaver O, Kracun S, Xu J,  
936 Sofroniew MV, Ellisman MH, Khakh BS. 2013. Imaging calcium microdomains  
937 within entire astrocyte territories and endfeet with GCaMPs expressed using  
938 adeno-associated viruses. *J Gen Physiol* **141**: 633-647.

939 Sompol P, Furman JL, Pleiss MM, Kraner SD, Artiushin IA, Batten SR, Quintero JE,  
940 Simmerman LA, Beckett TL, Lovell MA, Murphy MP, Gerhardt GA, Norris CM.  
941 2017. Calcineurin/NFAT Signaling in Activated Astrocytes Drives Network  
942 Hyperexcitability in Abeta-Bearing Mice. *J Neurosci* **37**: 6132-6148.

943 Soumpasis DM. 1983. Theoretical analysis of fluorescence photobleaching recovery  
944 experiments. *Biophys J* **41**: 95-97.

945 Stoppini L, Buchs PA, Muller D. 1991. A simple method for organotypic cultures of  
946 nervous tissue. *Journal of Neuroscience Methods* **37**: 173-182.

947 Stoyan D. 2006. On estimators of the nearest neighbour distance distribution function  
948 for stationary point processes. *Metrika* **64**: 139-150.

949 Sylantsev S, Rusakov DA. 2013. Sub-millisecond ligand probing of cell receptors with  
950 multiple solution exchange. *Nature Protocols* **8**: 1299-1306.

951 Tence M, Ezan P, Amigou E, Giaume C. 2012. Increased interaction of connexin43  
952 with zonula occludens-1 during inhibition of gap junctions by G protein-coupled  
953 receptor agonists. *Cell Signal* **24**: 86-98.

954 Underhill SM, Wheeler DS, Amara SG. 2015. Differential regulation of two isoforms of  
955 the glial glutamate transporter EAAT2 by DLG1 and CaMKII. *J Neurosci* **35**: 5260-  
956 5270.

957 van de Linde S, Loschberger A, Klein T, Heidbreder M, Wolter S, Heilemann M, Sauer  
958 M. 2011. Direct stochastic optical reconstruction microscopy with standard  
959 fluorescent probes. *Nature Protocols* **6**: 991-1009.

960 Verkhratsky A, Nedergaard M. 2018. Physiology of Astroglia. *Physiol Rev* **98**: 239-  
961 389.

962 Wadiche JI, Amara SG, Kavanaugh MP. 1995a. Ion fluxes associated with excitatory  
963 amino acid transport. *Neuron* **15**: 721-728.

964 Wadiche JI, Arriza JL, Amara SG, Kavanaugh MP. 1995b. Kinetics of a human  
965 glutamate transporter. *Neuron* **14**: 1019-1027.

966 Woods G, Zito K. 2008. Preparation of gene gun bullets and biolistic transfection of  
967 neurons in slice culture. *J Vis Exp*.

968 Zheng K, Rusakov DA. 2015. Efficient integration of synaptic events by NMDA  
969 receptors in three-dimensional neuropil. *Biophysical Journal* **108**: 2457-2464.

970 Zheng K, Scimemi A, Rusakov DA. 2008. Receptor actions of synaptically released  
971 glutamate: the role of transporters on the scale from nanometers to microns.  
972 *Biophysical Journal* **95**: 4584-4596.

973  
974

## 975 **ADDITIONAL FILE**

976 Each file named 'Figure X\_and\_Supplement\_Source.xlsx' in Excel format contains  
977 original numerical data presented in Figure X.

978

979

## 980 **FIGURE LEGENDS**

981

982 **Figure 1. Superecliptic synaptophluorin GLT1-SEP enables monitoring of cell**  
983 **membrane and cytosolic fractions of glial glutamate transporters.**

984 (A) Diagram illustrating molecular composition of GLT1-SEP.

985 (B) Functional probing of wild-type GLT1-SEP (SEP) probe expressed in HEK cells  
986 shows a prominent current response to glutamate application, similar to that wild-type  
987 GLT-1 (WT); top diagram, theta-glass pressure pipette application; traces, one-cell  
988 examples ( $V_h = -70$  mV).

989 (C) Summary of tests shown in (A): normalised current-voltage dependencies of GLT-  
990 1 (mean  $\pm$  SEM;  $n = 8$ ) and GLT1-SEP ( $n = 4$ ) are indistinguishable; current values  
991 normalised at  $V_h = -70$  mV (absolute values  $194 \pm 29$  pA and  $81 \pm 10$  pA for GLT-1  
992 and GLT1-SEP, respectively).

993 (D) Transient acidification ( $\sim 10$  s pH 5.5 puff, upper row) suppresses cell-surface GLT1-  
994 SEP fluorescence whereas transient membrane  $\text{NH}_4^+$  permeation ( $\sim 10$  s  $\text{NH}_4\text{Cl}$  puff,  
995 lower row) reveals the cytosolic fraction of GLT1-SEP; one-cell example.

996 (E) Time course of fluorescence intensity averaged over the cell soma (magenta) or all  
997 processes (green) in the test shown in (C).

998 (F) Average cell-surface fraction  $R$  of GLT1-SEP (summary of experiments shown in  
999 D-E); dots, individual cells (connecting lines indicate the same cell); grey bars,  
1000 average values ( $R$  mean  $\pm$  SEM:  $0.51 \pm 0.15$ ,  $n = 6$  for somata;  $0.72 \pm 0.18$ ,  $n = 8$  for  
1001 processes; soma boundaries in two cells were poorly defined).

1002

1003 **Figure 1 - source data 1. Original data readout for Figure 1D, E, F, Figure 1 -**  
1004 **figure supplement 2B, D and Figure 1 - figure supplement 3B-C.**

1005

1006 **Figure 1 - figure supplement 1. Testing glutamate transport function and the**  
1007 **membrane/ cytosol fraction ratio for GLT1-SEP.**

1008 (A) Summary of transporter current recordings in wild-type GLT-1 (black) and GLT1-  
1009 SEP (red) expressing HEK cells, as indicated; absolute current values are shown.

1010 (B) Diagram illustrating the kinetics of exchange between the plasma membrane  
1011 fraction (concentration  $C_m$ ) and the cytosol fraction (concentration  $C_{in}$ ) of GLT1-SEP;  
1012  $k_1$  and  $k_{-1}$ , kinetic constants, as shown.

1013 (C) *Right*, kinetic equations describing membrane-cytosol exchange for GLT1-SEP;  
1014  $C_{tot}$ , total concentration of GLT1-SEP;  $R$ , is the (equilibrated) membrane fraction of  
1015 GLT1-SEP, measured experimentally (Figure 1).

1016

1017 **Figure 1 - figure supplement 2. Expression of GLT1, GLT1-SEP, and GLT1ΔC-**  
1018 **SEP in HEK cells.**

1019 (A) Examples of immunostaining of GLT1 in HEK 293T cells co-transfected with  
1020 plasmids coding GLT1 or GLT1-SEP under CMV promoter together with mRFP1  
1021 under  $\beta$ -actin promoter (control reference) in a 2:1 ratio. Total GLT1 was  
1022 immunolabelled using an antibody which recognises the C-terminus of GLT1 or GLT1-  
1023 SEP.

1024 (B) Expression levels of GLT1 and GLT1-SEP (mean  $\pm$  SEM, data normalised against  
1025 average GLT1 level in HEK293T cells expressing GLT1a as 100%); numbers of cells  
1026 shown; \*\*\*  $p < 0.001$  (two-sample  $t$ -test; three cultures per condition).

1027 (C) Western blot of HEK 293T cells co-transfected with plasmids coding GLT1, GLT1-  
1028 SEP, or GLT1ΔC-SEP under CMV promoter together with mRFP1 under  $\beta$ -actin  
1029 promoter in a 2:1 ratio. Cell Lysates were analysed using Western Blotting with anti  
1030 GLT1 antibody directed against the extracellular loop, thus recognizing GLT1 and  
1031 GLT1-SEP and GLT1ΔC-SEP. Total protein loading was checked using anti- $\alpha$ -Tubulin  
1032 antibody.

1033 (D) Summary of Western blot (mean  $\pm$  SEM): GLT1 signal shown normalised to the  $\alpha$ -  
1034 Tubulin signal; open circles, individual cultures.

1035

1036 **Figure 1 - figure supplement 3. Relative expression GLT1, GLT1-SEP, and**  
1037 **GLT1ΔC-SEP astrocytes.**

1038 (A) Examples of immunostaining for GFP in astroglia transfected with GLT1-SEP or  
1039 GLT1ΔC-SEP, and total GLT1 (using an antibody which recognises C-terminus of both  
1040 endogenous GLT1 and transfected GLT1-SEP, but not GLT1ΔC-SEP), as indicated.

1041 (B) Quantitative summary of immunostaining (mean  $\pm$  SEM, data normalised against  
1042 the average GLT1 staining of non-transfected cells as 100%; dots, individual  
1043 astrocytes), for GLT1-SEP and GLT1ΔC-SEP transfected cells (three separate  
1044 cultures), as indicated; \*\*\*  $p < 0.005$ ; \*\*  $p < 0.01$  (two-sample  $t$ -test).

1045 (C) Control measurement of fluorescence intensity (mean  $\pm$  SEM) indicating a stable  
1046 expression level of endogenous GLT1 in non-transfected cells for cultures transfected  
1047 either with GLT1-SEP or with GLT1 $\Delta$ C-SEP (three cultures each; dots, individual  
1048 astrocytes).

1049

1050 **Figure 2. Whole-cell FRAP reveals the kinetics of the GLT1-SEP membrane**  
1051 **surface turnover.**

1052 (A) One-cell example illustrating FRAP protocol; upper left, DIC+SEP channel image;  
1053 serial images, GLT1-SEP channel at different time points (indicated) after a  
1054 photobleaching pulse ( $t = 0$  s); dashed green spiral illustrates application of the  
1055 tornado laser linescan mode; dashed red circle, laser-photobleached region; dotted  
1056 orange circles, example of ROIs.

1057 (B) Time course (mean  $\pm$  SEM,  $n = 27$  ROIs in  $N = 9$  cells) of the GLT1-SEP  
1058 fluorescence intensity within the photobleached region (as in A), normalised against  
1059 the baseline value. Red line, best-fit GLT1-SEP FRAP kinetics incorporating cytosolic  
1060 protein fraction ( $C_{in}$ ), membrane-surface turnover constants ( $k_1$  and  $k_{-1}$ ) and the  
1061 residual photobleaching constant ( $k_b$ ; not shown); see text and Figure 2S for further  
1062 detail.

1063 (C) Experiment as in (B), but with the with the C-terminus deleted mutant GLT1 $\Delta$ C-  
1064 SEP expressed in astroglia ( $n = 25$  ROIs in  $N = 8$  cells); other notations as in (B).

1065 (D) Two characteristic examples illustrating cellular distribution of surface-bound  
1066 fraction of GLT1-SEP (green, SEP<sub>out</sub>) and its intracellular fraction (red, SEP<sub>in</sub>) in live  
1067 individual astroglia.

1068

1069 **Figure 2 - source data 1. Original data readout for Figure 2B-C.**

1070

1071 **Figure 2 - figure supplement 1. Establishing the kinetics of whole-cell FRAP for**  
1072 **GLT1-SEP molecules in astrocytes.**

1073 *FRAP reactions* diagram reflects exchange (turnover) between membrane cytosol  
1074 fractions of non-bleached GLT1-SEP molecules, with  $C_{mem}^f$  and  $C_{in}^f$  standing for their  
1075 relative concentrations, respectively, and residual bleaching of the membrane fraction  
1076 adding to the bleached membrane fraction  $C_{mem}^b$ .  $k_1$ ,  $k_{-1}$ , and  $k_b$  are the kinetic  
1077 constants, as indicated.

1078 *Kinetics equations* describe the FRAP reactions in partial derivatives for  $C_{mem}^f$  and  $C_{in}^f$ .  
1079 The corresponding solution includes two unknown constants,  $C_0$  and  $C_1$ , which are  
1080 determined using *Initial and boundary conditions*, leading to the expression of

1081 *Fluorescence kinetics*. Other notations:  $\beta = \left(\frac{1}{R} - 1\right)$  where  $R$  is total (bleached and  
1082 non-bleached) membrane fraction of GLT1-SEP, as in Figure 1 - figure supplement 1.

1083

1084 **Figure 3. Distribution of GLT-1 species in relation to postsynaptic densities in**  
1085 **the astroglial membrane: A super-resolution SMLM analysis.**

1086 (A) Wide-field fluorescent images (examples) illustrating antibody labelled GLT1  
1087 species (green channel) and postsynaptic density protein PSD95 (magenta), as  
1088 indicated, in mixed astroglia-neuron cultures. See Figure S3A for macroscopic views.

1089 (B) SMLM nano-localisation maps (examples) depicting individual labelled GLT1  
1090 species (green), as indicated, and PSD95 (magenta) molecules. Top row, ROIs shown  
1091 as the corresponding yellow squares in (A); bottom row, ROIs shown as red squares  
1092 in the top row.

1093 (C) Red line (5 nm bins): distribution  $D(r)$  of nearest-neighbour (N-N) distances  $r$   
1094 between labelled GLT1 species and clusters of PSD95 molecules (PSD95 clusters  
1095 represent >50 particles <100 nm apart). Grey line: theoretical distribution  
1096  $D(r) = 1 - \exp(-\lambda\pi r^2)$  that corresponds to the Poisson point process (evenly random  
1097 scatter) with the same surface density of PSD95 clusters  $\lambda$  as sampled experimentally.  
1098 Experimental  $\lambda$  values were:  $67 \mu\text{m}^{-2}$  (WT GLT-1),  $15.5 \mu\text{m}^{-2}$  (GLT1-SEP), and  $22.2$   
1099  $\mu\text{m}^{-2}$  (GLT1 $\Delta$ -SEP); see Materials and Methods for detail.

1100

1101 **Figure 3 - source data 1. Original data readout for Figure 3C and Figure 3 - figure**  
1102 **supplement 1B.**

1103

1104 **Figure 3 - figure supplement 1. Distribution of GLT-1 species in the astroglial**  
1105 **membrane: macroscopic wide-field view and super-resolution SMLM analysis.**

1106 (A) Wide-field fluorescent images (examples) displaying antibody labelled GLT1  
1107 species (green channel) and postsynaptic density protein PSD95 (magenta), as  
1108 indicated, in mixed astroglia-neuron cultures. See Figure 3 for higher magnification.

1109 (B) SMLM analyses (see Figure 3 for single-molecule maps): Distribution  $D(r)$  of  
1110 nearest-neighbour (N-N) distances  $r$  among labelled GLT1 species (green line, 5 nm  
1111 bins), and the theoretical distribution for the Poisson point process (evenly random  
1112 scatter,  $D(r) = 1 - \exp(-\lambda\pi r^2)$ ) with the same surface density  $\lambda$  (grey line);  
1113 experimentally sampled  $\lambda$  values were  $324 \mu\text{m}^{-2}$  (WT GLT-1),  $67 \mu\text{m}^{-2}$  (GLT1-SEP),  
1114 and  $2938 \mu\text{m}^{-2}$  (GLT1 $\Delta$ C-SEP); a shift to the left for the green versus grey line  
1115 indicates significant clustering. See Materials and Methods for detail.

1116



1117 **Figure 4. Microscopic-ROI FRAP probes lateral membrane mobility of GLT1-SEP**  
1118 **in cultured astroglia.**

1119 (A) One-cell example as seen in GLT1-SEP + DIC channel (left), with a selected area  
1120 (dotted rectangle) illustrating a circular, 2.06  $\mu\text{m}$  wide FRAP spot (dotted circle, right).

1121 (B) Diagram, the paired-sample FRAP protocol, in which two trials are carried out in  
1122 succession, to account for any non-specific, time-dependent drift in FRAP kinetics.  
1123 Plots, one-cell example of the paired-sample FRAP test, with the first and second trial  
1124 data are shown in blue and green, respectively; arrow, bleaching pulse ( $\lambda_{\text{x}}^{2\text{p}} = 690 \text{ nm}$ ,  
1125 10-15 mW under the objective, duration 46 ms); fluorescence ROI, photobleaching  
1126 spot as in (A).

1127 (C) Diagram illustrating the paired-sample FRAP protocol, which includes both control  
1128 and glutamate application cycles; FRAP kinetics under glutamate application could be  
1129 corrected for non-specific drift by using the control cycle data.

1130 (D) *Left*, average time course of the GLT1-SEP FRAP (dots and shade: mean  $\pm$  95%  
1131 confidence interval, here and thereafter) in baseline conditions (black) and upon  
1132 glutamate application (250 ms puff 200 ms before the photobleaching pulse lured);  
1133 asterisk,  $p < 0.05$  ( $n = 69$  FRAP spots in  $N = 13$  cells). *Right*, FRAP time course (mean  
1134 values) fitted with the Soumpasis FRAP equation for (see main text) for control and  
1135 glutamate tests. Best-fit GLT1-SEP diffusion coefficient  $D$  is shown for control (Cntrl)  
1136 and glutamate puff (Glu) trials, as indicated.

1137 (E) Average FRAP time course in control and glutamate-puff tests carried out with the  
1138 C-terminus deleted mutant CLT1 $\Delta$ C-SEP, as indicated ( $n = 30$  FRAP spots in  $N = 7$   
1139 cells); other notation as in (D).

1140 (F) Average FRAP time course in control and glutamate-puff tests in the presence of  
1141 AMPA and metabotropic glutamate receptor (mGluR) blockers ( $n = 34$  FRAP spots in  
1142  $N = 7$  cells): MPEP (1 mM), LY341495 (30 nM), YM298198 (0.3  $\mu\text{M}$ ); NBQX (10  $\mu\text{M}$ )  
1143 was added to suppress network hyper-excitability under LY341495; other notation as  
1144 in (D).

1145 (G) Average FRAP time course in control conditions and after the ATP pressure puff  
1146 (100  $\mu\text{M}$ , 250 ms duration 200 ms before bleaching start, no glutamate), as indicated  
1147 ( $n = 14$  FRAP spots in  $N = 4$  cells); other notation as in (D).

1148 (H) Control test: Average FRAP time course in control conditions and under surface  
1149 cross-linkage by anti-GFP antibody, as indicated ( $n = 13$  FRAP spots in  $N = 2$  cells);  
1150 other notation as in (D).

1151

1152 **Figure 4 - source data 1. Original data readout for Figure 4B, D-H.**

1153

1154 **Figure 4 - figure supplement 1. Microscopic-ROI FRAP probes lateral membrane**  
1155 **mobility of GLT1-SEP in cultured astroglia.**

1156 (A) One-cell example of FRAP kinetics at four trials (two paired-trial FRAP stages);  
1157 time-lapse images of a cell fragment with a FRAP spot (dotted red circle), at selected  
1158 time points before and after the photobleaching pulses (at  $t = 0$ ), as indicated.  
1159 (B) Time course of FRAP for the four consecutive trials shown in (A), as indicated.

1160

1161 **Figure 5. Microscopic-ROI FRAP probes lateral membrane mobility of astroglial**  
1162 **GLT1-SEP in organotypic hippocampal slices.**

1163 (A) Example of astroglia in an organotypic slice, seen in GLT1-SEP, tdTomato, and  
1164 merge+DIC channel, as indicated.

1165 (B) One-slice example of boosted excitatory activity (field potential recording, CA1  
1166 area) induced by the application of GABA<sub>A</sub> receptor blocker Bicuculine and the  
1167 potassium channel blocker 4-AP, as indicated.

1168 (C) Average time course of the GLT1-SEP FRAP (dots and shade: mean  $\pm$  95%  
1169 confidence interval, here and thereafter) in baseline conditions (black), Bicuculine+4-  
1170 AP application (red), and after sodium channel blockade by TTX (magenta), as  
1171 indicated;  $p < 0.05$  ( $n = 72$  FRAP spots in  $N = 15$  cells). *Right*, FRAP time course  
1172 (mean values) fitted with the Soumpasis FRAP equation for (see main text) for control  
1173 and glutamate tests. Best-fit GLT1-SEP diffusion coefficient  $D^*$  (Soumpasis FRAP fit)  
1174 is shown for control (Cntrl), Bicuculine+4-AP application (4AP) and TTX trials, as  
1175 indicated.

1176 (D) Average FRAP time course for the C-terminus deleted mutant GLT1 $\Delta$ C-SEP, as  
1177 indicated; other notation as in (C).

1178 (E) Average FRAP time course in the presence of metabotropic glutamate receptor  
1179 blockers ( $n = 33$  FRAP spots in  $N = 8$  cells): MPEP (1  $\mu$ M), LY341495 (30 nM),  
1180 YM298198 (0.3  $\mu$ M), and NBQX (10  $\mu$ M); other notation as in (C).

1181 (F) Average FRAP time course in the presence of intracellular BAPTA ( $n = 48$  FRAP  
1182 spots in  $N = 10$  cells); other notation as in (C).

1183 (G) Average FRAP time course under the calcineurin (phosphatase) blockade by  
1184 FK506 (1  $\mu$ M;  $n = 31$  FRAP spots in  $N = 6$  cells); other notation as in (C).

1185 (H) Average FRAP time course in the presence of the broad-range kinase activity  
1186 blocker Staurosporine (100 nM); \* $p < 0.05$  ( $n = 45$  FRAP spots in  $N = 8$  cells) other  
1187 notation as in (C).

1188

1189 **Figure 5 - source data 1. Original data readout for Figure 5C-H and Figure 5 -**  
1190 **figure supplement 1A-B.**

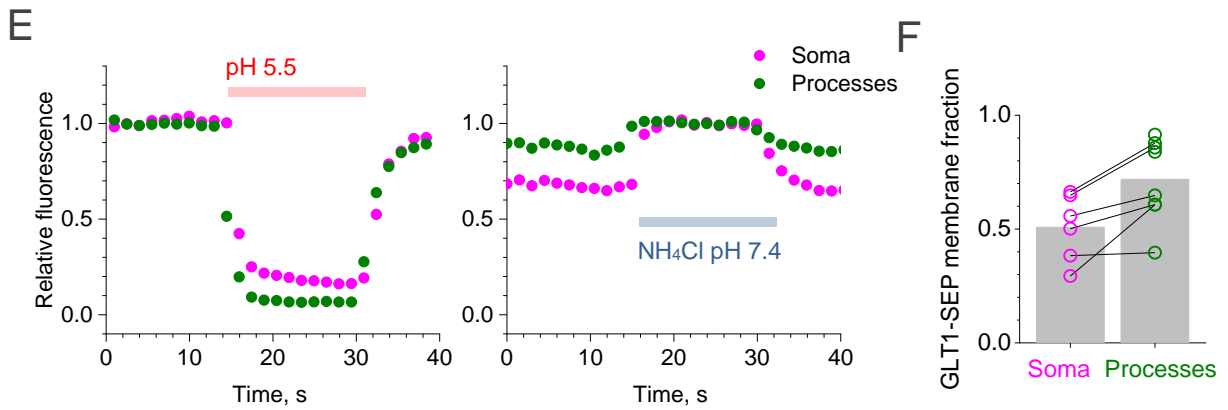
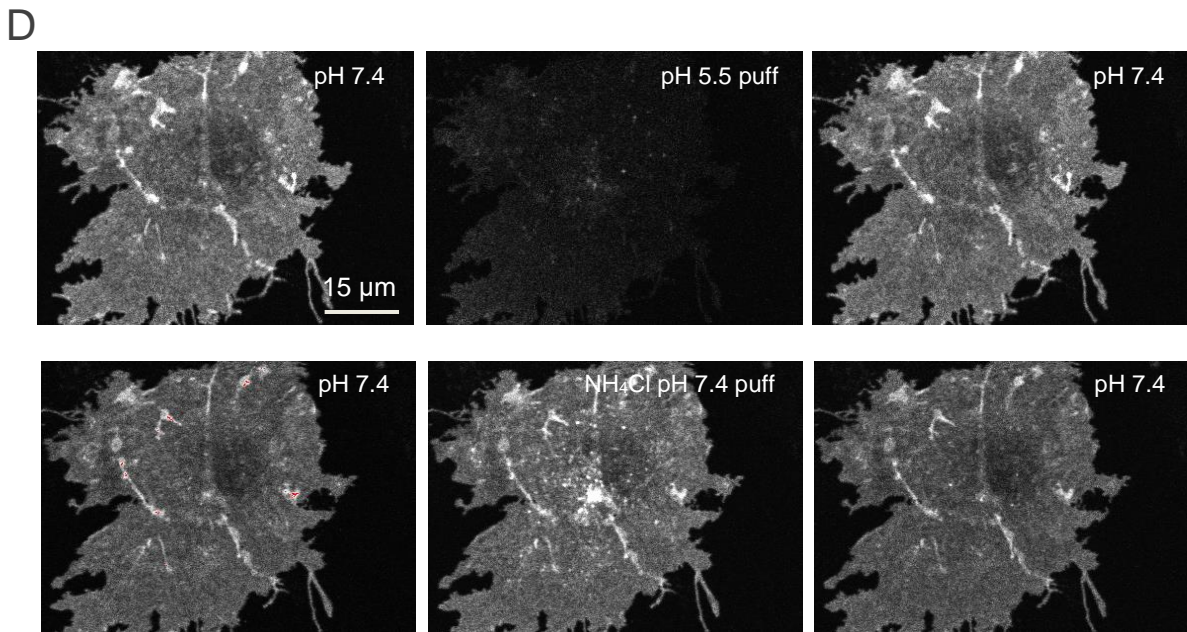
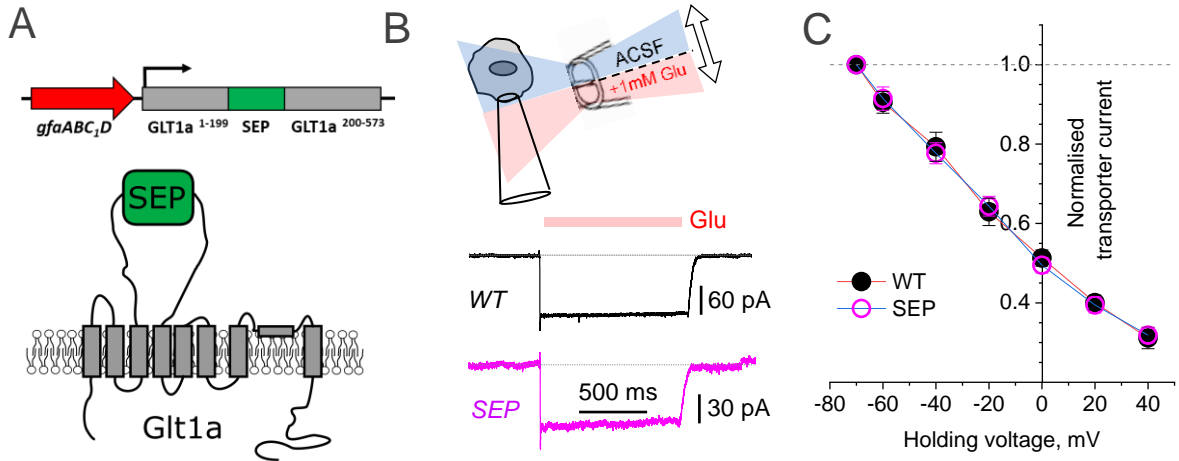
1191

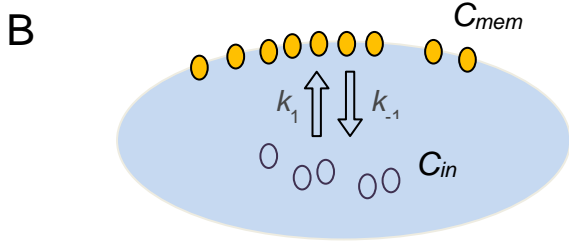
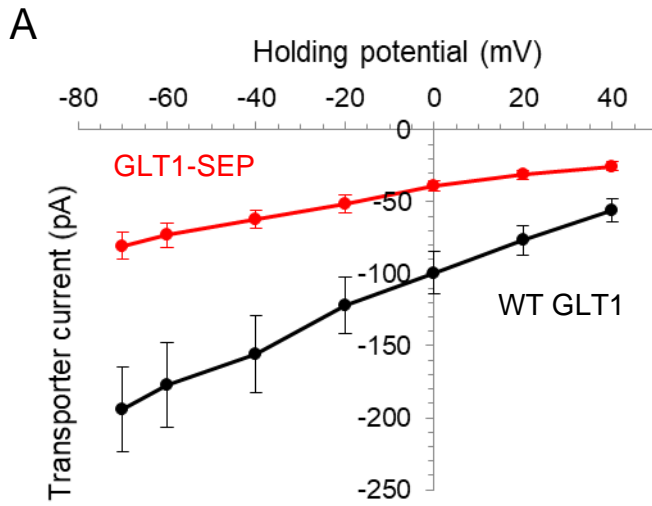
1192 **Figure 5 - figure supplement 1. Control tests for microscopic-ROI FRAP probing**  
1193 **of lateral membrane mobility of GLT1-SEP in organotypic hippocampal slices.**

1194 (A) Average time course of the truncated transmembrane protein (C-terminal  
1195 transmembrane anchoring domain of platelet-derived growth factor receptor) in fusion  
1196 with SEP (dots and shade: mean  $\pm$  95% confidence interval, here and thereafter), in  
1197 baseline conditions (black) and after the Bicuculine+4-AP application (red; n = 44  
1198 FRAP spots in N = 11 cells).

1199 (B) Average FRAP time course in the presence of drugs vehicle – 0.2% DMSO  
1200 baseline conditions (black) and after the Bicuculine+4-AP application (red); \*, p < 0.05  
1201 (n = 49 FRAP spots in N = 13 cells); other notation as in (A).

1202





**C**

$$C_{in} \xrightleftharpoons[k_{-1}]{k_1} C_{mem};$$

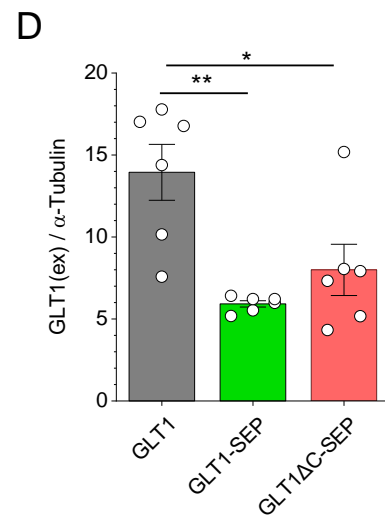
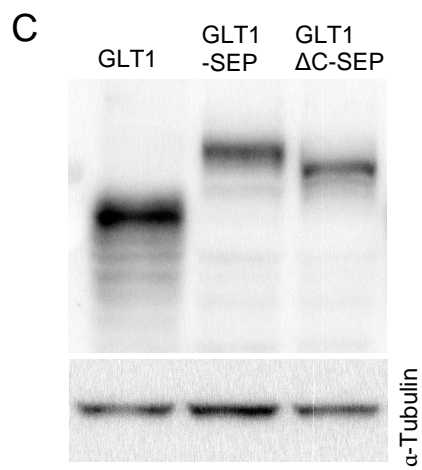
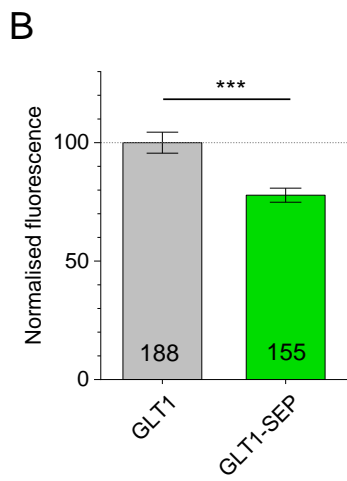
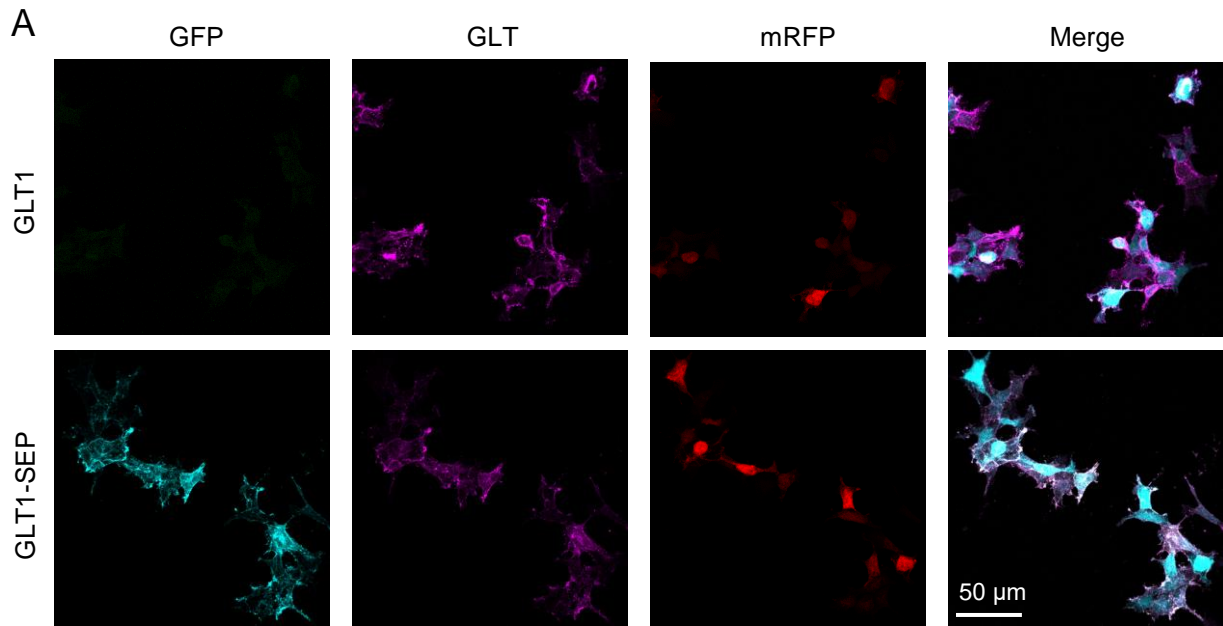
$$C_{in} + C_{mem} = C_{tot} = const;$$

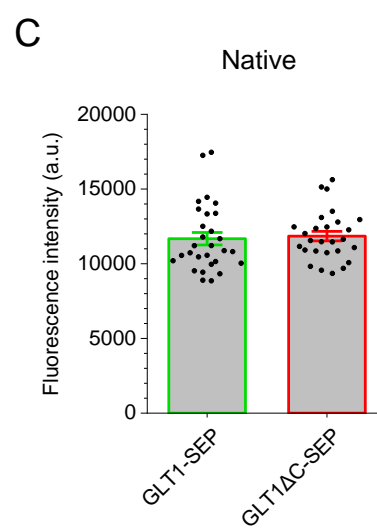
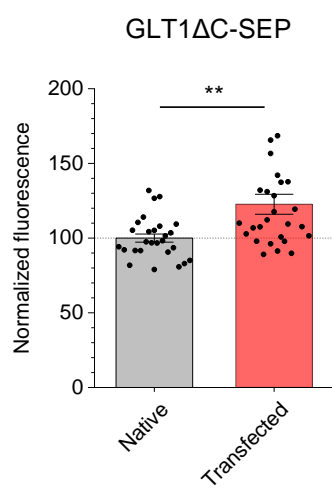
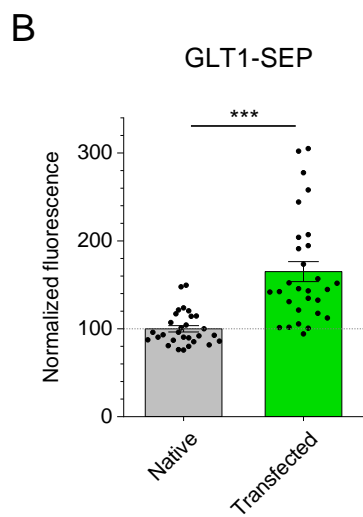
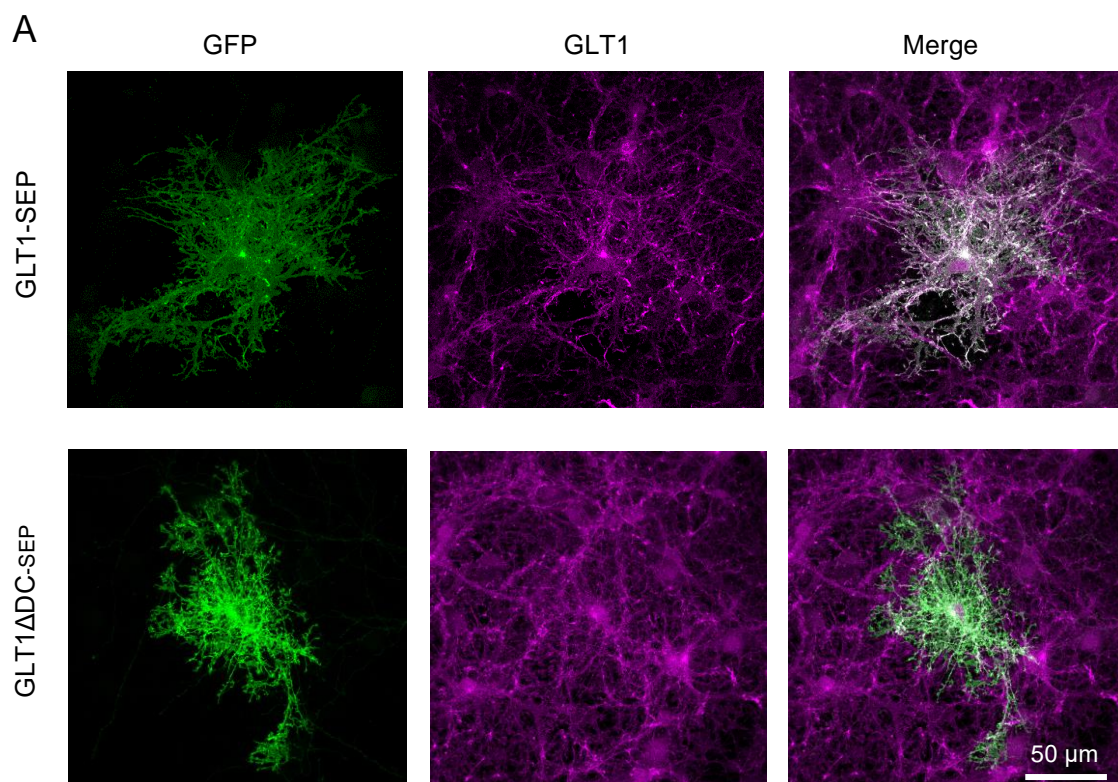
$$\frac{\partial C_{mem}}{\partial t} = k_1 C_{in} - k_{-1} C_{mem};$$

$$\left. \frac{\partial C_{mem}}{\partial t} \right|_{t \rightarrow \infty} = 0;$$

$$\frac{C_{mem}}{C_{tot}} = \frac{k_1}{k_1 + k_{-1}} = R \text{ (measured);}$$

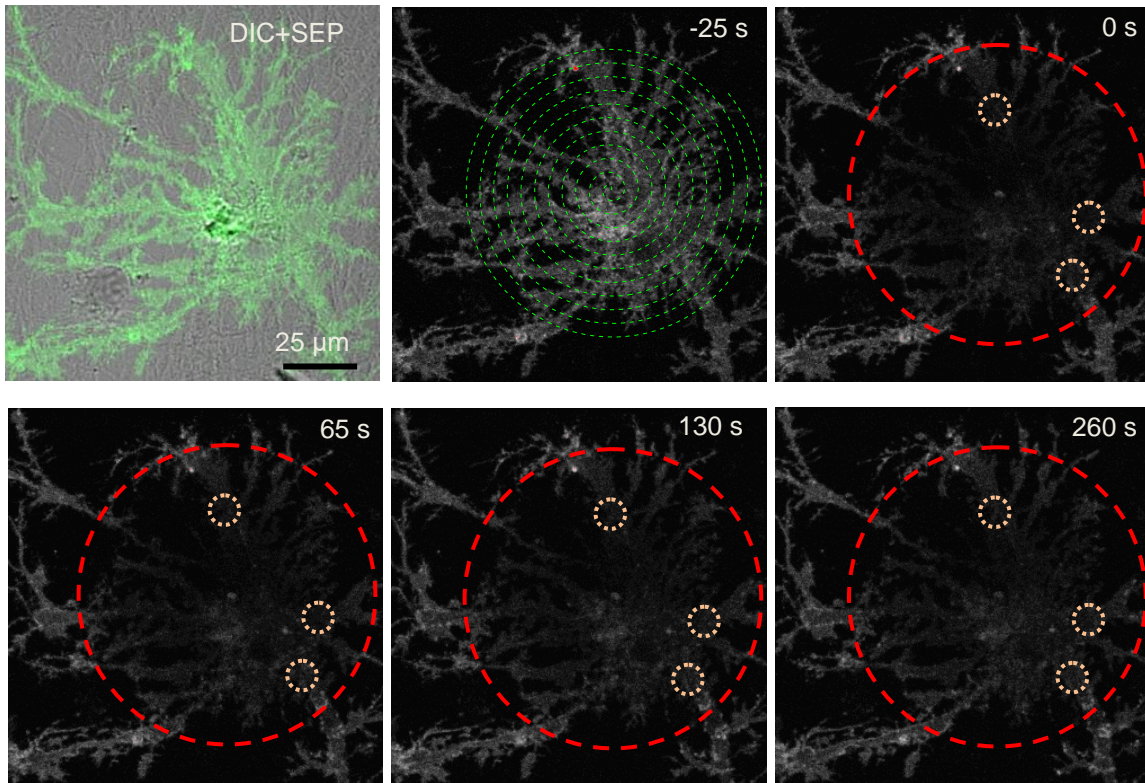
$$k_{-1} = \left( \frac{1}{R} - 1 \right) k_1 = \beta k_1$$



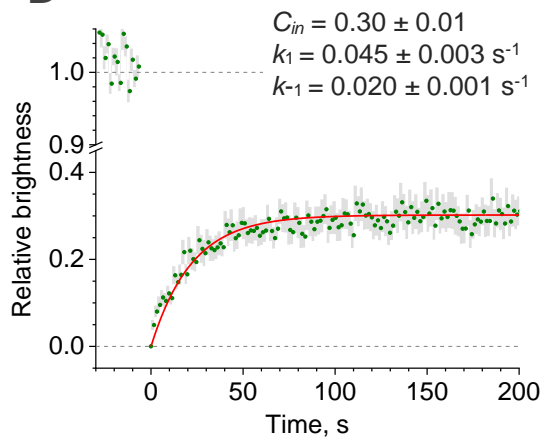




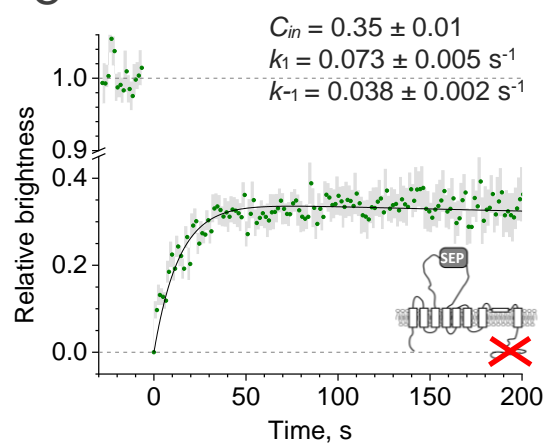
A



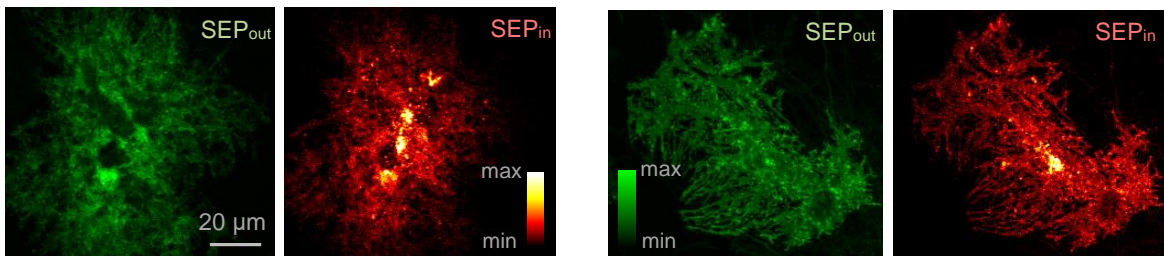
B



C

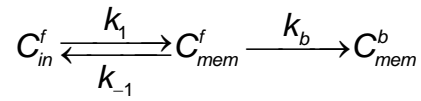


D





*FRAP reactions*



*Kinetic equations*

$$\frac{\partial C_{in}^f}{\partial t} = \beta k_1 C_{mem}^f - k_1 C_{in}^f \text{ hence } C_{in}^f = \beta C_{mem}^f - C_0 e^{-k_1 t};$$

$$\frac{\partial C_{mem}^f}{\partial t} = k_1 C_{in}^f - \beta k_1 C_{mem}^f - k_b C_{mem}^f \text{ hence}$$

$$\frac{\partial C_{mem}^f}{\partial t} = -k_1 C_0 e^{-k_1 t} - k_b C_{mem}^f \text{ hence}$$

$$C_{mem}^f = C_1 e^{-k_b t} - \frac{k_1}{k_b - k_1} C_0 e^{-k_1 t};$$

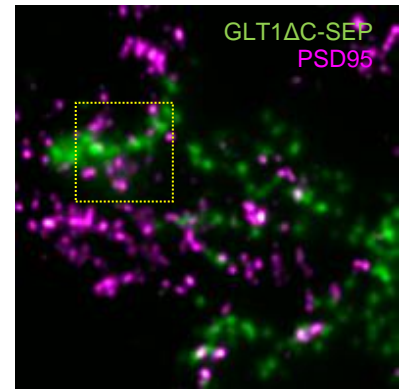
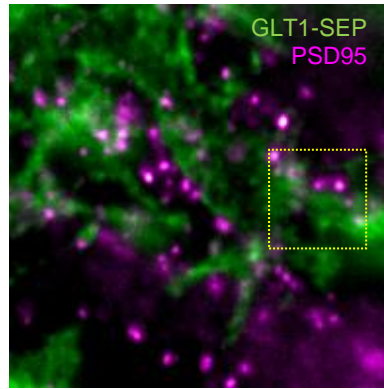
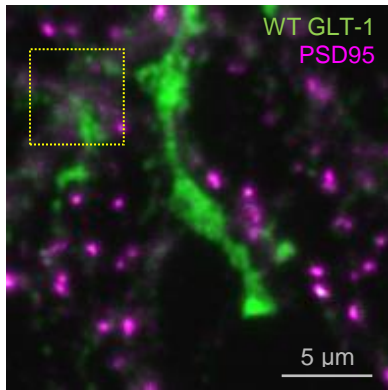
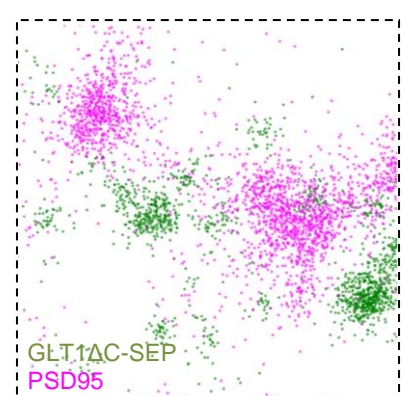
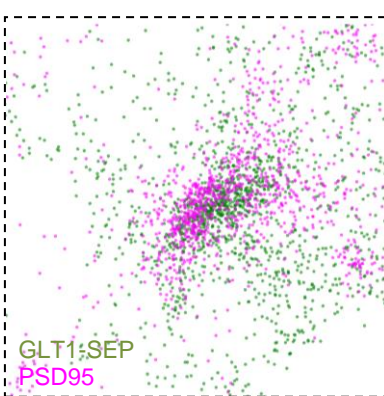
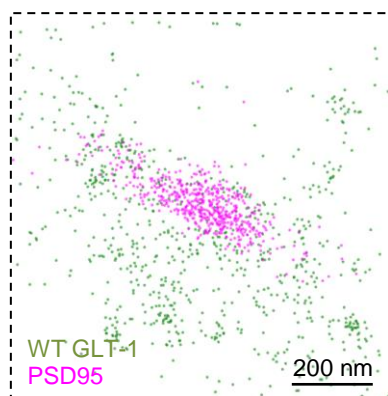
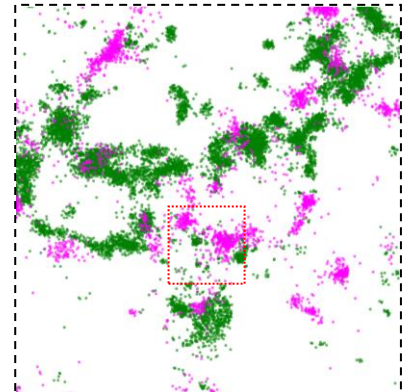
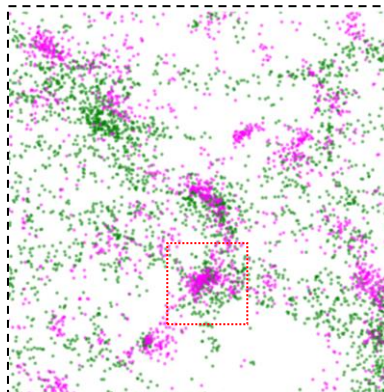
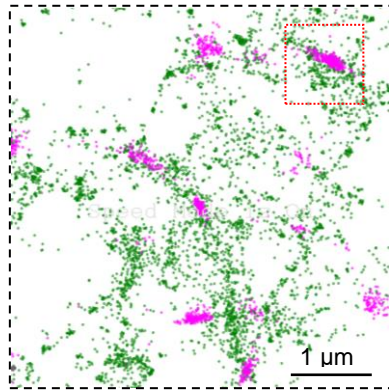
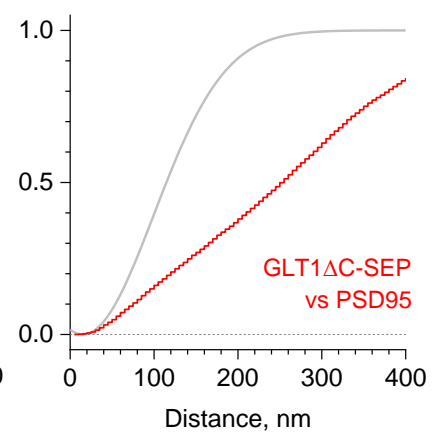
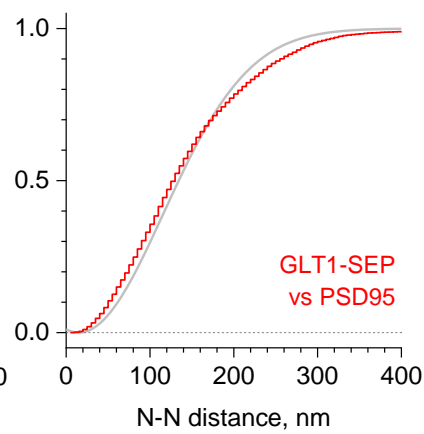
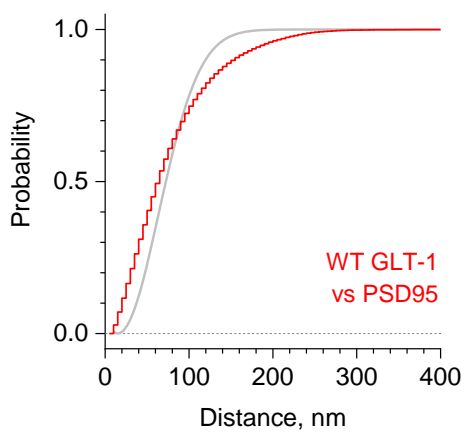
*Initial and boundary (limiting) conditions*

$$C_{mem}^f \Big|_{t=0} = 0 \text{ hence } C_{mem}^f = \frac{k_1}{k_b - k_1} C_0 (e^{-k_b t} - e^{-k_1 t});$$

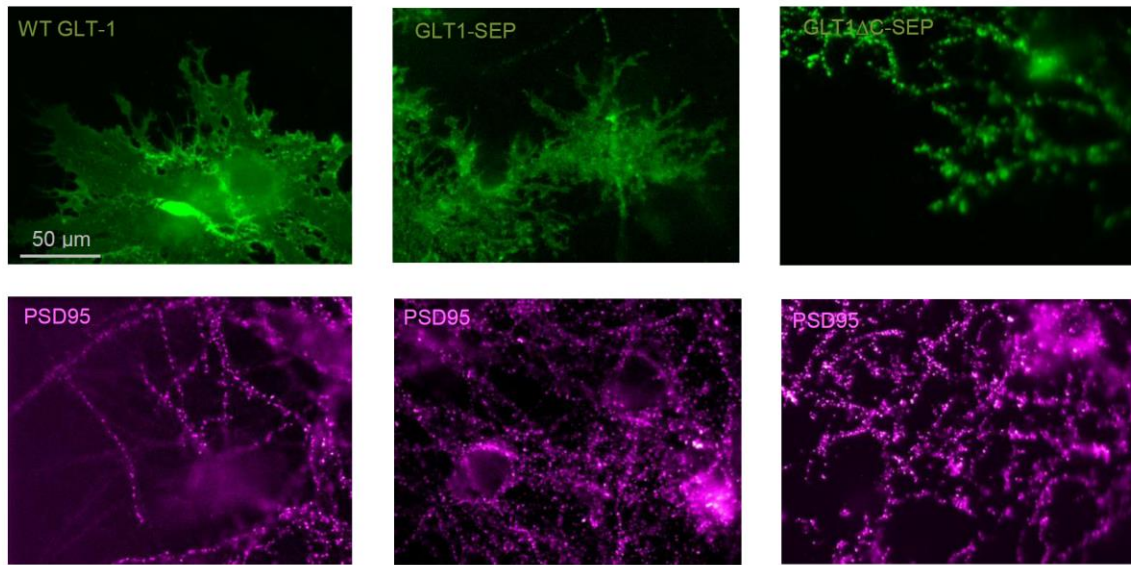
$$C_{mem}^f \Big|_{k_b=0, t \rightarrow \infty} = RC_{in} \text{ hence}$$

*Fluorescence kinetics*

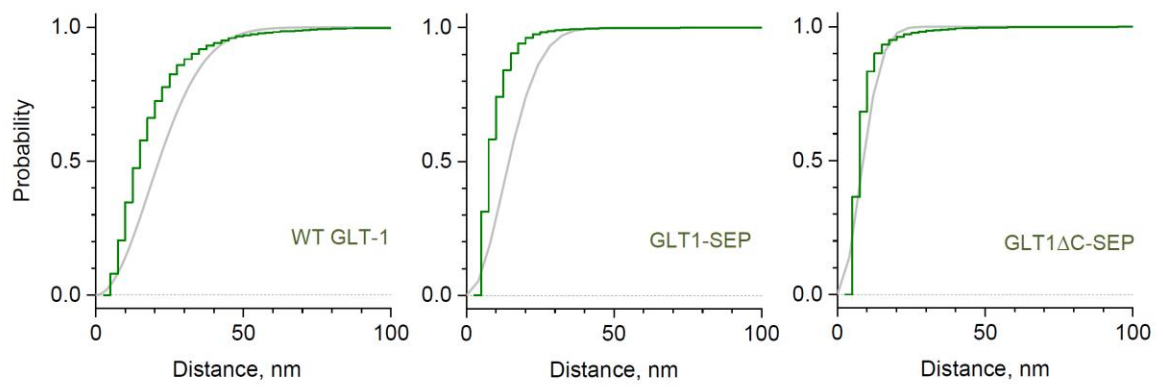
$$C_{mem}^f = RC_{in} (e^{-k_b t} - e^{-k_1 t})$$

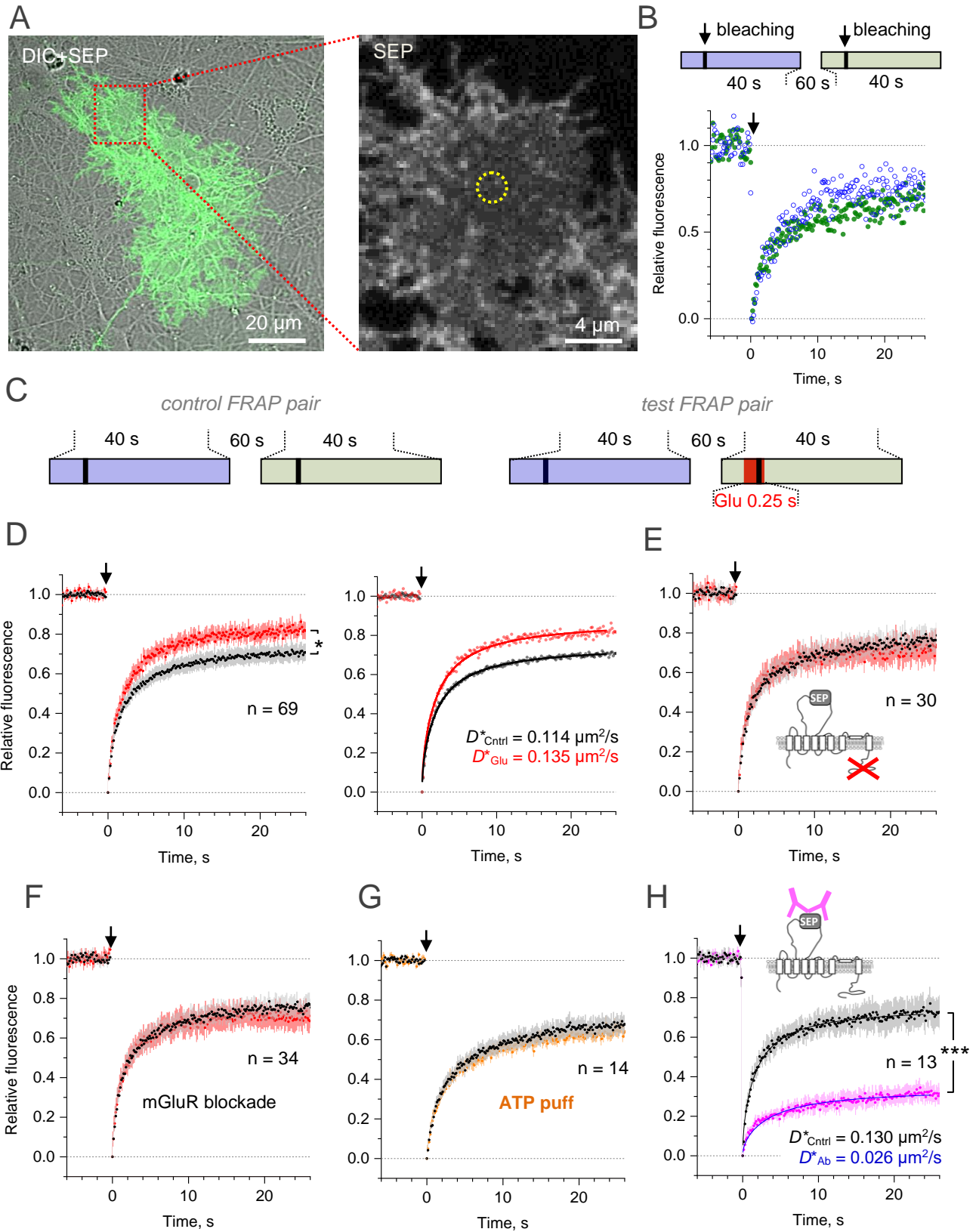
**A****B****C**

A

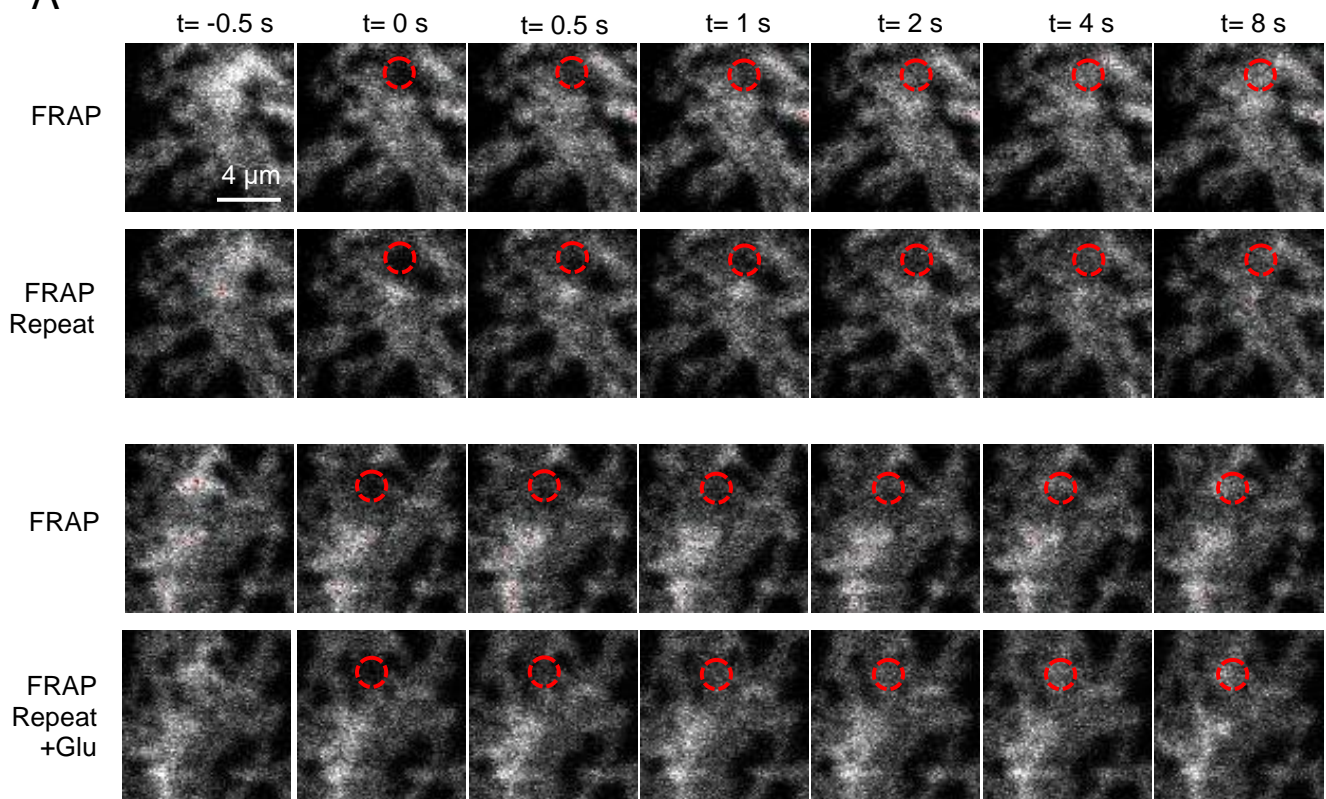
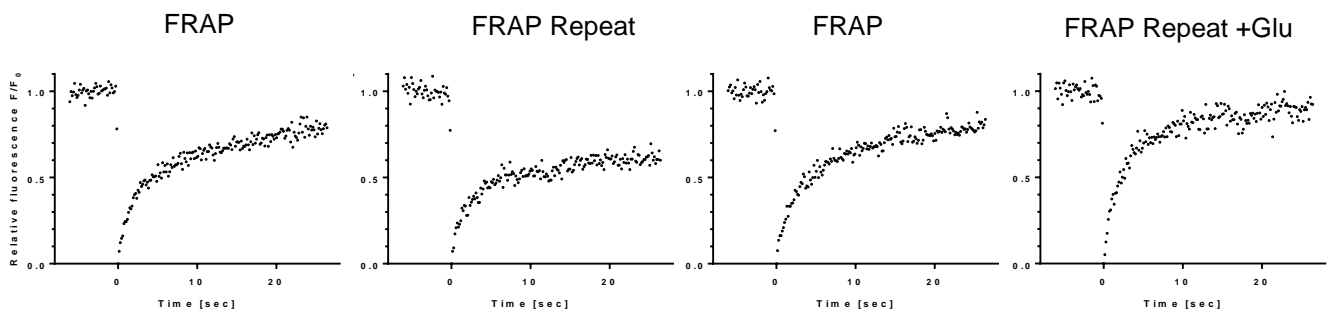


B

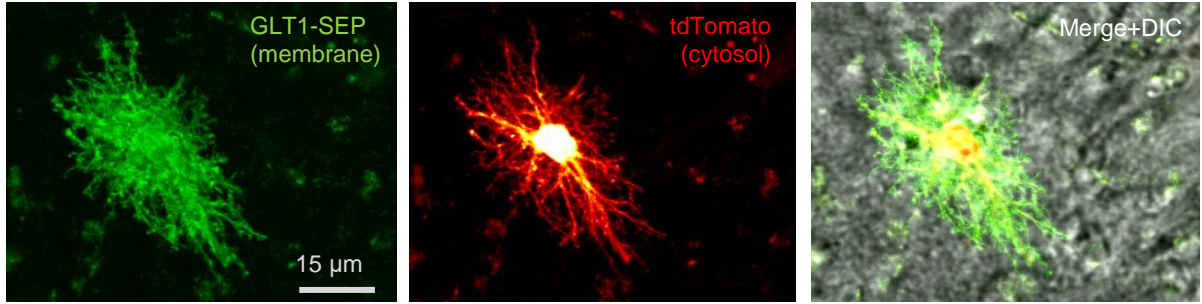




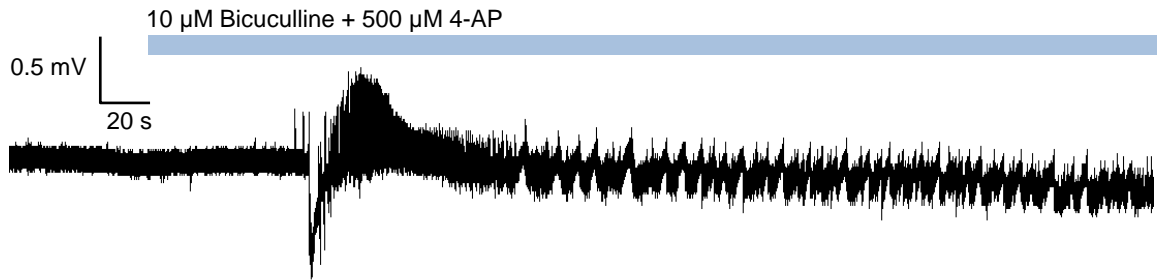


**A****B**

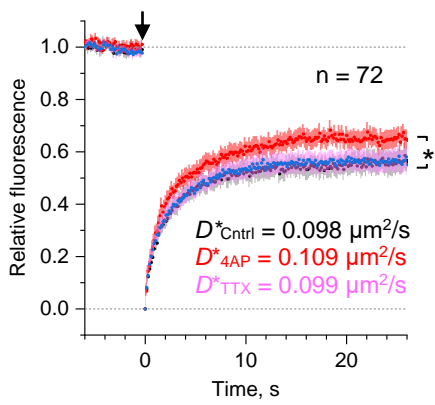
A



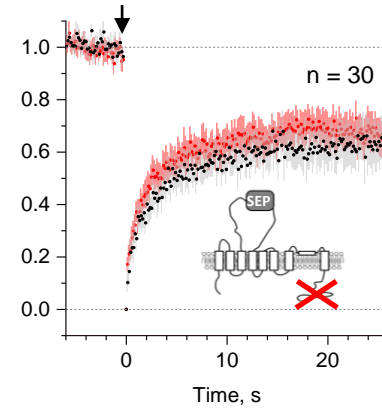
B



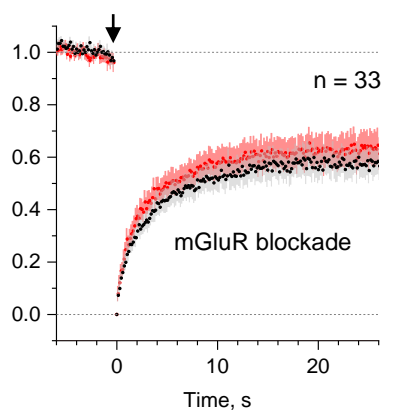
C



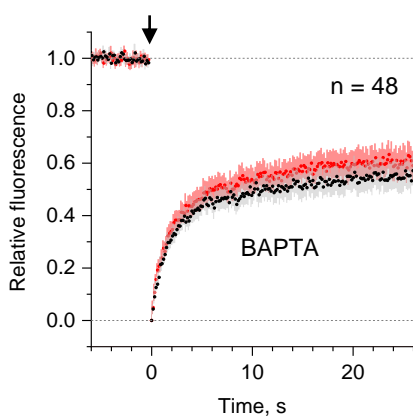
D



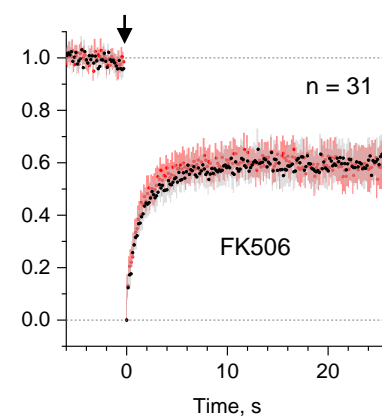
E



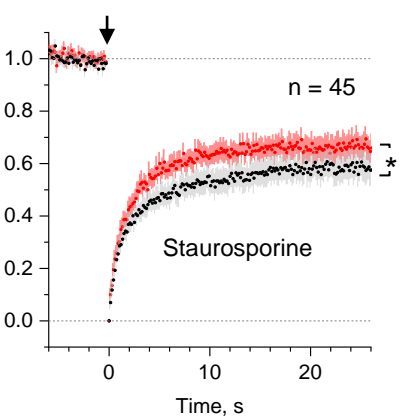
F



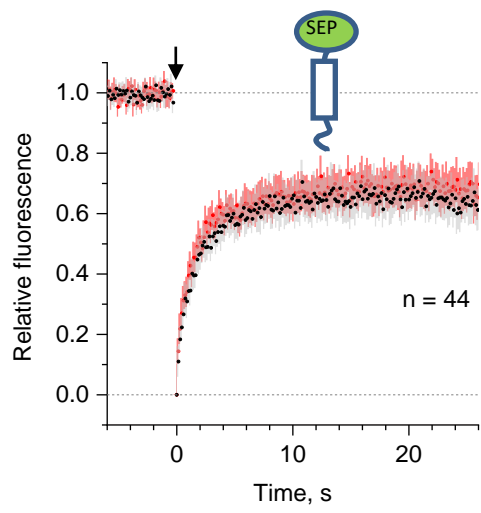
G



H



A



B

